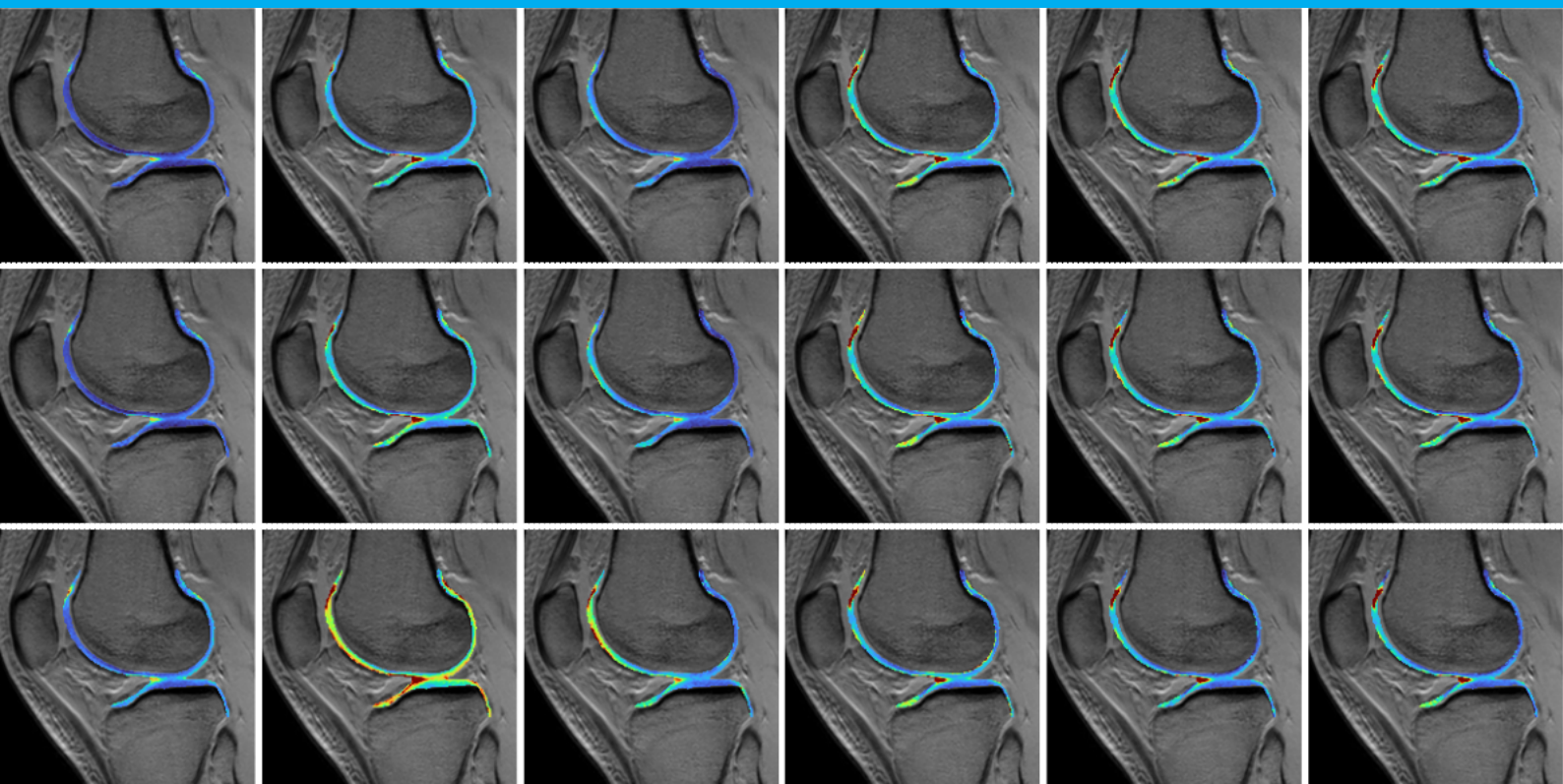


Parametric Relaxation Along a Fictitious Field (pRAFF) Pulse for Robust Quantitative MRI

A Parameterized Exploration of the
Subadiabatic and Adiabatic Regimes
for Radiofrequency Pulses Design

R.C. Naaktgeboren



Parametric Relaxation Along a Fictitious Field (pRAFF) Pulse for Robust Quantitative MRI

A Parameterized Exploration of the
Subadiabatic and Adiabatic Regimes
for Radiofrequency Pulses Design

by

R.C. Naaktgeboren

To obtain the degree of master of science
in *Applied Physics*
at the Delft University of Technology,
to be defended publicly on Tuesday March 28, 2023 at 15:00.

Project duration:	August 15, 2022 – March 28, 2023	
Project committee:	Dr. S. Weingärtner, C. Coletti, MSc.,	TU Delft, supervisor TU Delft, daily supervisor
Thesis committee:	Dr. F.M. Vos, Dr. I.E. Zadeh,	TU Delft TU Delft

Preface

In front of you lies the final report *Parametric Relaxation Along a Fictitious Field (pRAFF) Pulse for Robust Quantitative MRI*. This research was carried out to obtain the degree of master of science in Applied Physics at the Delft University of Technology.

From August 2022 to March 2023, I have been working on understanding Magnetic Resonance Imaging (MRI) and Relaxation Along a Fictitious Field (RAFF) radiofrequency pulse design. I developed a new method to improve RAFF against field inhomogeneities based on simulations, phantom, and in vivo acquisitions. During this period, MRI scans were acquired with the 3T Ingenia Phillips MRI-scanner at the HollandPTC when I was part of the Magnetic Resonance Systems Lab (Mars Lab) in the Department of Imaging Physics at the Delft University of Technology. This report documents all the findings during this period, the used literature and the results obtained from the research.

I would like to thank the entire Mars Lab for their support and in particular, I want to thank my supervisors: Sebastian Weingärtner and Chiara Coletti for their advice and supervision during the entire project.

*R.C. Naaktgeboren
Delft, March 2023*

Abstract

Magnetic resonance imaging (MRI) is a clinical imaging technique that allows for non-invasive visualization inside the human body with excellent soft tissue contrast with a sub-millimeter resolution. Qualitative MRI is used to visually highlight normal or pathological components by exploiting the physical properties of different tissues. However, these acquisitions provide minimal consistency between scans, patients, and scanners. To address this issue, quantitative MRI (qMRI) provides absolute measures that give meaningful physical information about tissues, enabling objective comparisons. Relaxometry, a branch of qMRI that characterizes tissues through their magnetic relaxation properties, has been employed to quantitatively assess various diseases with different biomarkers in the past. However, certain radiofrequency (RF) pulses used to induce relaxation times weighting in the MRI signal are sensitive to field inhomogeneities, which makes consistent quantification of relaxation times difficult. In order to improve sensitivity and detect more diseases, better contrast mechanisms and biomarkers are crucial. One promising technique is Relaxation Along a Fictitious Field (RAFF), which may serve as a biomarker for a wide range of diseases due to its sensitivity to slow molecular motion in tissue. Currently, it has the downside of being sensitive to off-resonance and B_1^+ artifacts, which hampers clinical application. This project aims to develop novel contrasts for quantitative MRI by investigating the performance of adapted RF pulses. Ultimately, the goal is to reduce the susceptibility to off-resonance and B_1^+ artifacts for the RF pulses.

Chapter 2. The Principles of MRI

Chapter 2 gives an overview of the principles of MRI. To begin, the basics of MRI are introduced with a focus on the following topics: the source of the signal, image creation, and readout strategies. Secondly, the essential theory needed for the understanding of relaxation along a fictitious field (RAFF) is discussed: starting from relaxation in the first rotating frame of reference (RFR), then relaxation in the second RFR, adiabatic excitation pulses, and finally RAFF.

Chapter 3. First Findings of Off-resonance and B_1^+ Resilience of Parameterized RAFF Pulses

Chapter 3 describes the first approach proposing improved RAFF pulses against field inhomogeneities. These pulses are an extension of RAFF with one extra degree of freedom (DoF). The chapter was accepted to the 2023 ISMRM annual meeting as a conference abstract with the following synopsis: Spin-lock (SL) relaxation times can provide valuable biomarkers for pathological remodeling in tissue, but acquisition with constant-amplitude SL pulses is limited by the specific absorption rate (SAR) and high sensitivity to field inhomogeneities. Relaxation along a fictitious field (RAFF) can measure rotating-frame relaxation with reduced SAR burden. In this work, we evaluate RAFF's resilience against B_0 and B_1^+ field inhomogeneities. Introduced, yet another RAFF (yaRAFF) pulse for fictitious field spin-locking with increased effective field strength. Compared with RAFF, yaRAFF yields >5.9% reduced susceptibility for field inhomogeneities in simulations and phantom. yaRAFF at 3T maintained quantitative map quality at large off-resonances in phantom and in vivo.

Chapter 4. Final Findings of Off-resonance and B_1^+ Resilience of Parameterized RAFF Pulses

Chapter 4 reports the final findings of RAFF pulses optimization, based on 3 degrees of freedom. The proposed pRAFF pulse was tested against field inhomogeneities and compared to conventional RAFF pulses in phantoms and in-vivo. The chapter serves as the basis for a paper, currently under submission, with the following outline:

Purpose: Reducing the susceptibility to off-resonance and B_1^+ artifacts for Relaxation Along a Fictitious Field (RAFF) radiofrequency (RF) pulses.

Methods: Bloch simulations were performed to find the optimal preparation performance against B_0 and B_1^+ artifacts of newly proposed RAFF pulses, an extension of RAFF with three degrees of freedom (DoF). This

resulted in the optimal pulse. Phantom MRI acquisitions were acquired for several off-resonance and relative B_1^+ artifacts to validate the Bloch simulations. The preparation efficiency of the optimal and original RAFF pulse was compared in simulation and phantom. To study the parametric behavior of the new pulses, resilience against field inhomogeneities and to assess mapping quality, T_{RAFF} maps were acquired in the phantom, calf, and knee cartilage with a spGRE readout for off-resonances, relative B_1^+ artifacts, and combined field inhomogeneities across healthy subjects.

Results: The preparation performance in the phantom of the optimal and standard RAFF pulses are in agreement with the Bloch simulations. The optimal pulse showed increased preparation efficiency compared to RAFF, 0.95 compared to 0.67, and a significant increase in the performance of relaxation time mapping was obtained. A 5 times higher B_1^+ and B_0 inhomogeneity resilience of 496 ± 14 Hz with respect to 104 ± 8 Hz was obtained in the calf, and similarly in the phantom. Likewise, relaxation time mapping of the knee cartilage showed increased field inhomogeneity tolerance without the loss of contrast. Indicated by the coefficient of variation within field inhomogeneities of 57% for RAFF compared to 11% for the optimal pulse, with minimal fluctuations across healthy subjects. In the knee cartilage, relaxation times of both pulses are in the same order: 50 ± 14 ms and 42 ± 11 ms, respectively the optimal and RAFF pulse.

Conclusion: The RAFF preparation pulse can be significantly improved against B_0 and B_1^+ inhomogeneities while maintaining the quantification of in vivo relaxation times in the calf and knee cartilage at 3T.

Contents

Preface	i
Abstract	ii
List of abbreviations	v
1 Introduction	1
2 The Principles of MRI	3
2.1 Magnetic Resonance Imaging Basics	3
2.1.1 Precession	3
2.1.2 Excitation Pulse	4
2.1.3 Relaxation	5
2.2 Rotating Frame Relaxation	8
2.2.1 Adiabatic RF Pulses	9
2.3 Relaxation Along a Fictitious Field	11
3 First Findings of Off-resonance and B_1+ Resilience of RAFF Pulses	13
3.1 Introduction	13
3.2 Methods	13
3.3 Results	13
3.4 Discussion	14
3.5 Conclusion	14
3.6 Figures	15
4 Final Findings of Off-resonance and B_1+ Resilience of RAFF Pulses	17
4.1 Introduction	17
4.2 Methods	18
4.2.1 RF Pulse Design	18
4.3 Results	20
4.3.1 Bloch Simulations Results	20
4.3.2 B_0 and B_1^+ Inhomogeneities Resilience Results.	20
4.4 Discussion	21
4.5 Conclusions.	22
4.6 Supporting Information.	22
4.7 Figures	23
5 Outlook	34
Appendices	37
A Pulse Derivations	37
A.1 Problem: Constant Effective Field	37
A.2 Problem: Locked Effective Field or Constant Fictitious Field.	39
A.3 Problem: Constant Effective Field in the Second Rotating Frame	40
A.4 Problem: Equally Effective and Fictitious Field Strength or a Locked E-field	42

List of Abbreviations

B_0	Main magnetic field
B_1	The secondary magnetic field
M	Net magnetization vector
G_x, G_y and G_z	Gradient coils
M_x, M_y and M_z	Net magnetization vector components
AFP	Adiabatic Full-Passage
AM	Amplitude modulation
CNR	Contrast-to-noise ratio
CoV	Coefficient of variation
DoF	Degree of freedom
FID	Free induction decay
FM	Frequency modulation
MRI	Magnetic Resonance Imaging
pRAFF	parametric RAFF
RAFF	Relaxation Along a Fictitious Field
RF	Radiofrequency
RFR	Rotating frame of reference
ROI	Region of interest
SAR	Specific absorption rate
SL	Spin-lock
SNR	Signal-to-noise ratio
TE	Echo time
TR	Repetition time
TSL	Spin-lock time
yaRAFF	yet another RAFF

1

Introduction

Magnetic resonance imaging (MRI) is a non-invasive in vivo imaging technique with a sub-millimeter resolution, which is widely used in clinical settings to image inside the human body [1]. MRI uses strong magnetic fields to create images with good soft tissue contrast. Currently, there is no evidence of any health risks associated with temporary exposure to MRI [2]. Unlike nuclear medicine and radiography, which are diagnostic imaging techniques that involve ionizing radiation.

Traditionally, MRI acquisitions have been qualitative and relied on the physical properties of tissues to visually emphasize healthy or abnormal components, rather than using quantitative values to represent the underlying properties of the tissues. Qualitative MRI acquisitions can be highly variable between different scanners, patients, and even between different scans. This is because the images are influenced by various factors such as signal-to-noise ratio (SNR), MRI hardware, and scanning protocols [3]. Quantitative MRI (qMRI) provides absolute measures that give meaningful physical information about tissues, which can be objectively compared [4] and show greater inter-site repeatability [5].

Relaxometry, the branch of qMRI characterizing tissues through their magnetic relaxation properties, has been used in the past to quantitatively assess numerous diseases with several biomarkers. During the MRI scans, each relaxation time functions as a marker describing its own underlying mechanism. For laboratory relaxation times (T_1 and T_2), T_1 links its properties to the extracellular water content [6] and T_2 is associated with collagen fiber orientation and tissue hydration [6]. Both relaxation times have shown their clinical value across the human body, for instance, in the brain, heart, and knee [5, 7, 6].

On top of laboratory relaxation times, have spin-lock (SL) relaxation times ($T_{1\rho}$) been proposed to be more insightful in cases of evaluating specific tissue properties and pathogenic changes [8]. Relaxation during SL describes the magnetization behaviour in a rotating frame of reference when the magnetization is locked along the radiofrequency (RF) pulse, whereas for T_1 and T_2 , relaxation takes respectively place along and perpendicular to the main magnetic field. Since $T_{1\rho}$ is sensitive to slow molecular motion interactions that occur between free water and macromolecular protons [9], its clinical value can be shown in early disease detection of for instance myocardial fibrosis [7], Alzheimer's disease [10], and post-traumatic osteoarthritis [9, 6], but it is predominantly used for cartilage imaging. Unfortunately, conventional $T_{1\rho}$ has the downside of having a high specific absorption rate (SAR) burden, which can cause tissue overheating when exposed to the RF pulses. On top of that, has conventional $T_{1\rho}$ a large susceptibility to field inhomogeneities [7], resulting that consistent measurements of relaxation times are challenging. Therefore, better contrast mechanisms and biomarkers are critical to increase sensitivity and detect additional diseases.

Relaxation Along a Fictitious Field (RAFF) is a promising method, that was developed to overcome the SAR limitations of conventional constant amplitude SL and has shown comparable sensitivity to slow molecular motion in tissue [8]. RAFF mimics a small energy gap with a locking field in the second rotating frame of reference, instead of the first rotating frame for $T_{1\rho}$ pulses. Currently, RAFF is not widely used in the clinic due to its susceptibility to B_0 and B_1^+ inhomogeneities [11].

The goal of this project is to investigate the performance of adapted radiofrequency (RF) pulses to develop novel contrasts for quantitative MRI. Eventually, to lower the sensitivity of RF pulses to off-resonance and B_1^+ artifacts, and RAFF will be the basis of the newly designed RF pulses. During the project, the newly designed RF pulses will be studied by performing numerical simulations, phantom, and in vivo measurements. To achieve the goal of improved RF pulses against field inhomogeneities the following questions will

be answered: Which pulse design has the least susceptibility to off-resonance and B_1^+ artifacts?; Which pulse design is favorable to get a large in vivo contrast-to-noise ratio (CNR)?

The structure of the report is as follows. First off, in [chapter 2](#), the basic theoretical background on magnetic resonance imaging, relaxation, rotating frame relaxation, adiabatic pulses, and relaxation along a fictitious field will be presented. After covering all the literature, the first findings are in [chapter 3](#). [Chapter 4](#) covers the final findings and evaluates the results. Lastly, a conclusion and outlook for further research are given in [chapter 5](#).

2

The Principles of MRI

2.1. Magnetic Resonance Imaging Basics

Magnetic resonance imaging is an imaging modality, which is used in clinical applications for disease detection throughout the human body [12]. The signal produced in MRI arises from protons and their intrinsic spin. Predominately, the protons of hydrogen atoms produce the signal. The signal is produced by billions of nuclei, which makes it possible to describe the magnetic resonance signal as a classical phenomenon, even though the spin of a nucleus is a quantum mechanical effect [1]. MR imaging makes use of a strong magnetic field, the main magnetic field (\mathbf{B}_0 [T]), to align the spins in the field. When the main magnetic field for MR imaging is turned on, an energy gap arises and the atomic nuclei have a preferred direction along the field. The alignment of the nuclei spins can be described by a net magnetization vector (\mathbf{M} [A/m]) [1]. This process of turning on \mathbf{B}_0 is schematically shown in figure 2.1. Only applying the main magnetic field and therefore creating a net magnetization is insufficient to create an image for medical applications. Thus, before being able to create an image one first has to consider the phenomenon of precession.

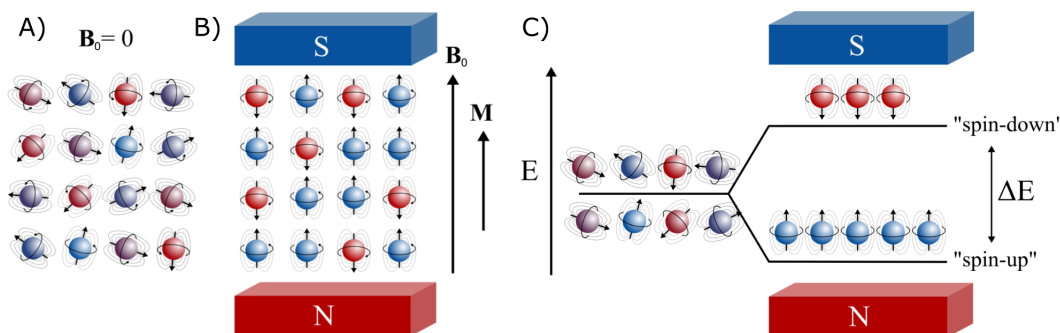


Figure 2.1: A) Randomly orientated spins, B) align with the main magnetic field (\mathbf{B}_0) and create a net magnetization (\mathbf{M}), C) \mathbf{M} arises due to the energy difference (ΔE) of the spin-down and spin-up state of the nuclei in the \mathbf{B}_0 field. Figure adapted from [13].

2.1.1. Precession

Precession is the resulting circular motion when an external force is applied to an object with angular momentum. As an example of precession, one could think of a rotating gyroscope or a spinning top in a gravitational field. In the case of MR imaging, the magnetization possesses angular momentum, due to the intrinsic spin, and therefore the magnetization rotates around the \mathbf{B}_0 field. The frequency at which the precession takes place in the main magnetic field is determined by equation 2.1 and is called the Larmor frequency, the most important frequency in MR imaging [1]:

$$\omega_0 = \gamma B_0, \quad (2.1)$$

where γ [Hz/T] is the gyromagnetic ratio, which differs for each specific nucleus. The most crucial gyromagnetic ratio to consider is the one of a hydrogen atom, which is 42.58 [Hz/T] [1].

During MR imaging the magnetization starts aligned with the \mathbf{B}_0 field at equilibrium. At this moment the magnetization does not yet precess around the \mathbf{B}_0 field. By tipping the magnetization with a second magnetic field (\mathbf{B}_1 [T]), \mathbf{M} will no longer be in equilibrium and starts a precession around the \mathbf{B}_0 field. To tip the magnetization the secondary magnetic field has to be applied with a frequency close to the Larmor frequency. In the case of matching frequencies, the energy transfer is the most effective and this is called on-resonance. When the second magnetic field is no longer present, the magnetization keeps precession around the main magnetic field because precession does not require nor does it dissipate energy [1]. The process is schematically shown in figure 2.2. Despite precession is not requiring energy, the magnetization will ultimately return to equilibrium, due to several processes, but first, a deeper understanding of the excitation pulse must be explored.

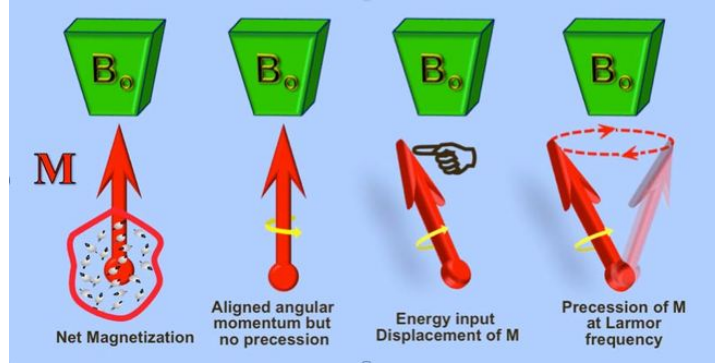


Figure 2.2: Tipping the aligned net magnetization, \mathbf{M} , out of equilibrium by applying a secondary magnetic field (\mathbf{B}_1). \mathbf{B}_1 is applied at the Larmor frequency. \mathbf{M} starts precessing around the main magnetic field (\mathbf{B}_0). [1]

2.1.2. Excitation Pulse

The excitation pulse, generated through a secondary magnetic field called the \mathbf{B}_1 field, is a radiofrequency (RF) pulse oscillating with the frequency ω_1 in the laboratory frame of reference. In the laboratory frame of reference, the laboratory and therefore the MRI-scanner is at rest (figure 2.3A). Conventionally, magnetization's behaviour has been examined in the first Rotating Frame of Reference (RFR). Since the first RFR is oscillating with ω_1 , the \mathbf{B}_1 field becomes stationary for constant \mathbf{B}_1 field amplitudes (figure 2.3B). First things first, in the laboratory frame of reference the magnetization behaviour can be described with equation 2.2 [13]. The Bloch equation describes the rotating behaviour of the magnetization around the magnetic field and the relaxation terms T_1 and T_2 , which will be discussed later. Magnetization trajectory simulations with the Bloch equations are referred to as Bloch simulations.

$$\frac{d\mathbf{M}(t)}{dt} = \frac{d}{dt} \begin{pmatrix} M_x \\ M_y \\ M_z \end{pmatrix} = \gamma \mathbf{M}(t) \times \mathbf{B}(t) - \begin{pmatrix} \frac{M_x(t)}{T_2} \\ \frac{M_y(t)}{T_2} \\ \frac{M_z(t) - M_0}{T_1} \end{pmatrix}, \quad (2.2)$$

with $\mathbf{B}(t)$ the total magnetic field, composed of \mathbf{B}_0 and the orthogonal \mathbf{B}_1 field (equation 2.3).

$$\mathbf{B}(t) = \mathbf{B}_0 + \mathbf{B}_1(t) = \begin{pmatrix} 0 \\ 0 \\ B_0 \end{pmatrix} + \begin{pmatrix} B_1 \cos(\omega_1 t) \\ B_1 \sin(\omega_1 t) \\ 0 \end{pmatrix} = \begin{pmatrix} B_1 \cos(\omega_1 t) \\ B_1 \sin(\omega_1 t) \\ B_0 \end{pmatrix}. \quad (2.3)$$

When transforming from the laboratory frame to the first RFR, the behaviour of the magnetization can still be described with Bloch equations, but the total magnetic field becomes the effective magnetic field and for the moment relaxation terms are omitted (equation 2.4) [13].

$$\frac{d\mathbf{M}(t)}{dt} = \gamma \mathbf{M}(t) \times \mathbf{B}_{\text{eff}}(t) = \gamma \mathbf{M}(t) \times \begin{pmatrix} B_1 \\ 0 \\ \Delta B_1 \end{pmatrix} = \gamma \mathbf{M}(t) \times \begin{pmatrix} B_1 \\ 0 \\ B_0 \left(1 - \frac{\omega_1}{\omega_0}\right) \end{pmatrix}. \quad (2.4)$$

Here $\Delta B_1 (= \Delta\omega_1 / \gamma$ [T]), is the off-resonance frequency with respect to the Larmor frequency.

As an effect of the excitation pulse, the magnetization rotates over a certain angle, the flip angle (α_{FA} [°]). For time-dependent B_1 amplitudes, the flip angle is described with [13]:

$$\alpha_{FA}(T_p) = \int_0^{T_p} \gamma B_1(t) dt, \quad (2.5)$$

with T_p the pulse duration. For constant field amplitudes, this breaks down to a circular rotating around the magnetic field with $\alpha_{FA}(T_p) = \gamma B_1 T_p$ (figure 2.3). While the description holds true for the on-resonance case, the off-resonance case is more complex, as depicted in figure 2.3C. Due to the combination of B_1 and non-zero ΔB_1 components, as described by equation 2.4, the effective field ($B_{eff} = \omega_{eff}/\gamma$ [T]) is out of the plane. As a result of the magnetization precessing around the remaining effective field, it no longer flips into the transverse plane, which is demonstrated in figure 2.3B.

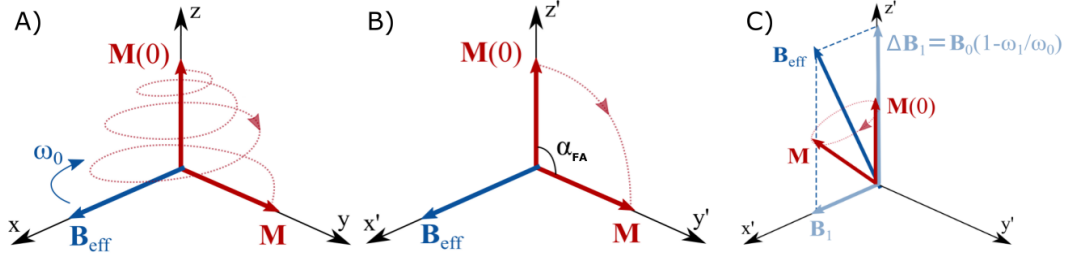


Figure 2.3: 90° flipping angle (α_{FA}) for on-resonance ($B_{eff} = B_1$, $\omega_1 = \omega_0$) in the A) laboratory and B) rotating frame of reference. The rotating frame is oscillating with ω_1 . C) Off-resonance ($\omega_1 \neq \omega_0$) excitation in the rotating frame of reference. The magnetization (M) no longer flips into the transverse plane. Figure adapted from [13].

2.1.3. Relaxation

After excitation, M relaxes back to equilibrium by dissipating the excess energy, due to interactions with other spins, collision, and molecular vibrations [1]. Relaxation is the source of contrast in MR imaging, as the magnetization vector is spatially affected differently, due to varying tissue properties and the environment. The obtained contrasts depend on the longitudinal (T_1 [s]) and transversal (T_2 [s]) relaxation times [1].

For longitudinal relaxation, the energy of the spins is dissipated to the surrounding lattice and is therefore known as spin-lattice relaxation. The energy is transferred between neighboring atoms and molecules through molecular interactions such as collisions, molecular vibrations, and electromagnetic interactions [14, 13]. The longitudinal magnetization approaches the equilibrium magnetization M_0 as the system recovers to equilibrium (figure 2.4). This process can be described with the Bloch equations and the relaxation terms (equation 2.2). The resulting behaviour is an exponential growth in time with T_1 as the characteristic time. After a 90° excitation, the exponential growth is described with equation 2.6. As a rule of thumb, the longitudinal magnetization is completely recovered after $\sim 5T_1$ (figure 2.4).

$$M_z(t) = M_0 \left(1 - e^{-t/T_1}\right). \quad (2.6)$$

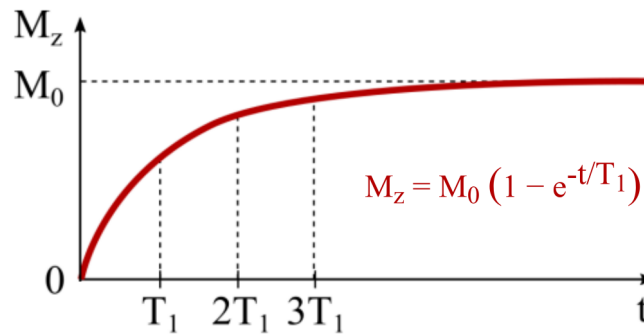


Figure 2.4: The exponential growth of M_z to equilibrium after 90° excitation. Figure adapted from [13].

The transverse magnetization (M_{xy}) is composed of coherently aligned spins after excitation. For transversal relaxation, spins start to dephase in the transverse plane, due to the presence of neighboring spins. The magnetic moment of neighboring spins gives small perturbations to the local magnetic field and causes spins to precess at different frequencies [13], resulting in destructive interference and causing a decay in the signal of M_{xy} towards zero (figure 2.5) with T_2 as the characteristic time. This decay is also known as free induction decay (FID) [15] and can be described by:

$$M_{xy}(t) = M_0 e^{-\frac{t}{T_2}}. \quad (2.7)$$

However, the effective signal loss of the transverse magnetization is a combination of two factors: T_2' (reversible) and T_2 (non-reversible) processes, combined as T_2^* (equation 2.8).

$$\frac{1}{T_2^*} = \frac{1}{T_2'} + \frac{1}{T_2}. \quad (2.8)$$

T_2' describes the effects of the inhomogeneities of the main magnetic field and heterogeneities in the susceptibility of tissues affecting the local precession. Both remain static over time and are therefore reversible [13]. This is visualized in figure 2.5, where applying a 180° refocusing pulse for the T_2' effects will completely rephase the spins at the echo time (TE). The time-dependent fluctuations are contained in T_2 , and thereby in T_2^* [13]. Besides, the dephasing effect of the magnetic moment interaction between neighbouring spins, one could think of random spin-spin interaction, due to Brownian motion as another source of T_2 relaxation. Since Brownian motion is a process of random molecular motion driven by temperature, it is an irreversible process. This makes T_2 non-reversible [15], and the effect on the magnetization signal can be seen in figure 2.5 where T_2^* is bounded by T_2 decay. T_1 and T_2 as contrast mechanisms and biomarkers are extensively discussed along the cartilage degeneration in qMRI.

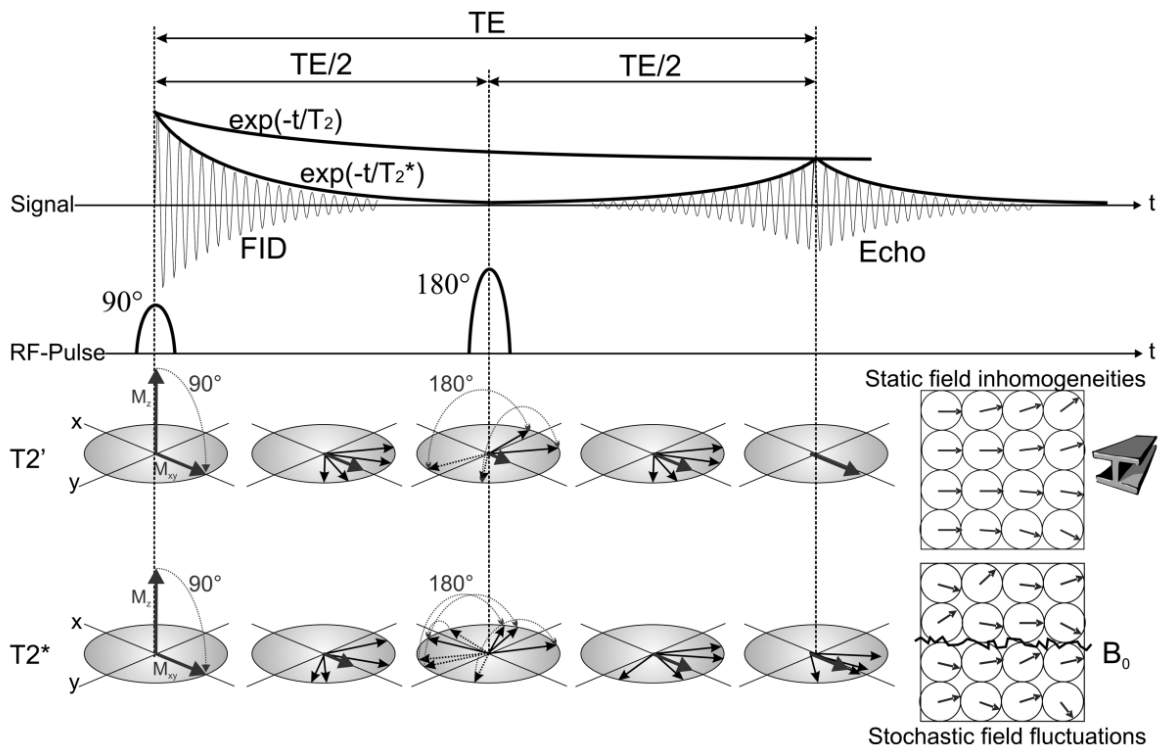


Figure 2.5: Exponential decay of transverse magnetization ($M_{xy}(t)$) after applying a 90° excitation in the transverse plane and a 180° refocusing pulse. The coherently aligned spins dephase after excitation, causing a free induction decay (FID) of T_2^* . The 180° refocusing pulse completely rephases the spins for T_2' components at the echo time (TE). The envelope of T_2^* decay is the magnetization signal in the laboratory frame, and the oscillating signal is the signal in the rotating frame of reference. T_2^* decay is bounded by T_2 decay, due to stochastic field fluctuations [15]

qMRI in Cartilage Degeneration

Osteoarthritis (OA) is widely thought of as a progressive disease that gradually deteriorates the cartilage within the joint and causes changes in the underlying bone structure [16]. This process can lead to pain, inflammation, and stiffness, as well as functional impairment and disability in those affected [17]. These symptoms become more apparent at an older age, limiting the quality of life [18]. Currently, no cure exists for OA, which makes the need for early diagnosis important to prevent further disease progression before irreversible damage occurs. However, radiography, the current gold standard for detecting cartilage degeneration, and conventional Magnetic Resonance Imaging (MRI) [19, 20], have generally not had repeated assessments of OA [16, 19]. In the initial stages of OA, molecular level changes are present in the cartilage, causing increased water content, and disruption of the collagen fibril network [19].

MRI modulations with laboratory relaxation as contrast mechanisms and biomarkers, T_1 and T_2 relaxation times, have shown clinical value in the early detection of diseases such as post-traumatic osteoarthritis [9, 6] and musculoskeletal diseases [20]. Both relaxation times have demonstrated their sensitivity based on their own characteristics, with T_1 being studied as a biomarker for osteoarthritis due to its sensitivity to extracellular water content. However, only a few studies have measured native T_1 times. Rautiainen et al. [6] found a strong correlation between prolonged T_1 relaxation and cartilage degeneration in a study modeling post-traumatic osteoarthritis in equine cartilage. In another study, Nissi et al. [21] measured various relaxation times for osteochondral defects in a bovine. They induced cartilage degeneration through enzyme injection to study altered collagen or proteoglycan content. All studied relaxation times were related to the destruction of the collagen network, and only native T_1 and gadolinium-enhanced T_1 showed sensitivity to impaired proteoglycan content.

Furthermore, T_2 has been studied for its relation to collagen fiber orientation and tissue hydration [6]. However, its behavior has been diverse in different studies, with Rautiainen et al. [6] showing a moderate correlation between T_2 proteoglycan content and the orientation of collagen fibers. Whereas Xia [22] showed the correlation between the direction character of T_2 and the collagen fibers. Hirose et al. [23], on the other hand, studied healthy cartilage and patients with OA, showing no changes between groups in T_2 relaxation and no directional behaviour of T_2 .

General in qMRI, relaxation time quantification is obtained by increasing the preparation time before the readout. In this way, the magnetization is sampled at several times during the relaxation process, which allows to fit of a model of the magnetization of for instance exponential growth or decay for T_1 and T_2 respectively. This brings us to the image readout, as each sampling requires a readout sequence.

Image Readout

The readout of an image is possible as precession is field strength dependent. In MR imaging, an image is created by applying linearly varying gradients (G_x , G_y and G_z) in the three Cartesian coordinates (figure 2.6A). These three gradients distort the main magnetic field. Because of the field dependence of the precession, each location in the field of view of the scanner is localized by a different frequency. In other words, spatial encoding is created by the gradients. The beauty of using linear varying gradients, is that each combination of gradients resembles a location in the Fourier domain or k-space (figure 2.6B). To completely fill the k-space, the readout sequence has to be repeated to stack up the domain line by line. For standard sequences, the time between repetitions is characterised by the repetition time (TR). Depending on the chosen combination of TR and TE, the contrast in an image can become either more T_1 or T_2 -weighted. Cased by the exponential recovery and decay of both relaxation effects [14]. For example for a spin-echo sequence, a combination of short TE and TR results in a T_1 -weighted image and for a long TR and TE the image becomes more T_2 -weighted [14]. Thus, by turning on a slice selective gradient in the z-direction, sending RF pulses with the \mathbf{B}_1 field, and recording the signal with varying spatial encoded gradients, an image can be obtained by applying an inverse Fourier transform of the k-space (figure 2.6). For a more detailed explanation of spatial encoding, one could read [1].

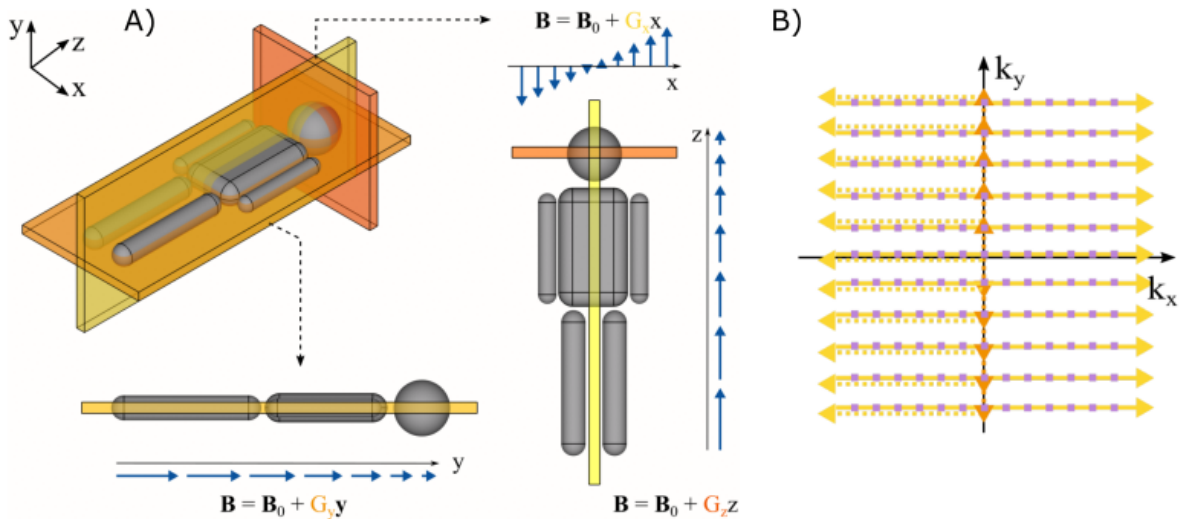


Figure 2.6: A) Linear varying gradients in all Cartesian directions. B) The sampling of the k-space for a selected 2D slice, where the strength of the gradient in the corresponding direction relates to the line in k-space. Figure adapted from [13].

2.2. Rotating Frame Relaxation

In addition to laboratory relaxation times (T_1 and T_2), there exist other relaxation times: rotating frame relaxation ($T_{1\rho}$ and $T_{2\rho}$). The relaxation naming containing the term "rho", implies the "rotating" frame. In cases, such as evaluating specific tissue properties and pathogenic changes, spin-lock relaxation in the rotating frame can be more insightful than laboratory frame relaxation times [8].

Spin-lock relaxation times ($T_{1\rho}$) have been suggested as a potentially valuable marker for several diseases, such as myocardial fibrosis [7], Alzheimer's disease [10] and cartilage degeneration [9]. This is because $T_{1\rho}$ is sensitive to slow molecular motion interactions between free water and macromolecular protons [9]. One could think of interactions in the Hz to kHz range compared to the kHz to MHz range for T_1 relaxation [24, 25]. Especially in the early detection of OA correlated with the molecular level changes present in the cartilage, gives a promising foundation for MRI rotating frame relaxometry.

In conventional MRI, the magnitude of the main magnetic field determines which speed of molecular motion gives rise to a contrast. This is because magnetic relaxation is dependent on the interaction of the magnetization with the surrounding molecules and energy transfer occurs around the Larmor frequency. The resulting energy gap is caused by the strength of the main magnetic field. A way to be sensitive to slow molecular motion, in conventional MRI, is to use a small \mathbf{B}_0 field. From a practical point of few, current scanners do not allow to change the main magnetic field strength. Even though decreasing the field strength would be possible, it comes at the cost of losing SNR, as the magnetization decreases in magnitude. Rotating frame relaxation, on the other hand, wants to mimic a small energy gap with a locking field in the first rotating frame of reference. This allows for sensitivity to slow molecular motion at all kinds of field strengths.

$T_{1\rho}$ acquisitions are typically performed by tipping the magnetization to the transverse plane and locking the magnetization along the effective field in the first RFR (figure 2.7B & C). During spin-lock a constant amplitude RF pulse is applied to fix the effective field along an axis in the first RFR. As illustrated in figure 2.7B, $T_{1\rho}$ relaxation occurs along the effective field for a certain spin-lock time (TSL), as opposed to T_1 relaxation, where relaxation occurs along the main magnetic field. There are several possible processes that might play a role for $T_{1\rho}$ relaxation, like dipolar interactions, chemical exchange, and diffusion effects [25]. To interact with these processes at clinical field strengths, usually, SL frequencies ranging from 100 to 500 Hz and spin-lock times between 2 and 100 ms are used [24]. Besides $T_{1\rho}$ relaxation, at the same time, $T_{2\rho}$ relaxation occurs along the perpendicular component of the effective field, similarly like T_2 relaxation does with respect to T_1 . However, $T_{2\rho}$ is hardly studied [24], and thus the focus will be on $T_{1\rho}$.

Unfortunately, conventional spin-lattice relaxation in the rotating frame has the downside of having a high specific absorption rate burden. SAR is a quantification of the energy absorbed by the human body when exposed to RF pulses. It is proportional to the RF pulse's squared amplitude multiplied by the pulse duration. Patients can be put in danger and irreparable harm can be done, due to too high SAR causing tissue

overheating. In addition to the high SAR burden, conventional $T_{1\rho}$ suffers from high susceptibility to field inhomogeneities [7], particularly at higher field strengths, preventing clinical use. Yet, improved resilience against field inhomogeneities was found for adiabatic $T_{1\rho}$ compared to conventional spin-lattice relaxation in the rotating frame [26].

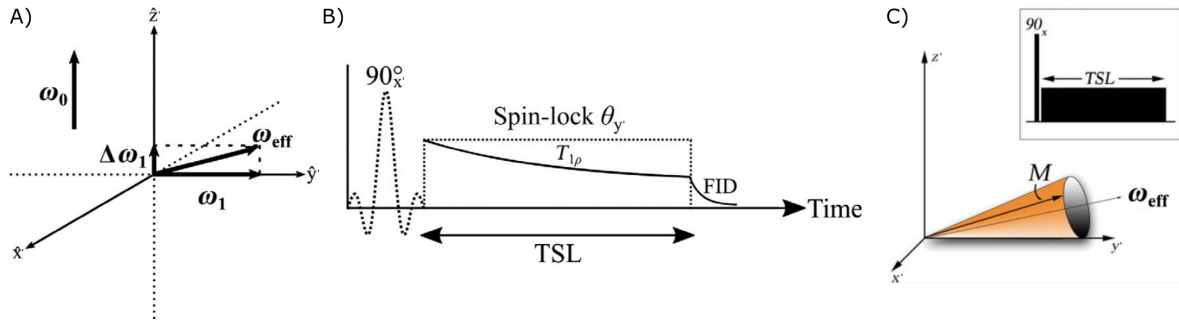


Figure 2.7: A) Shows the rotating frame with the locking field (ω_{eff}) for $T_{1\rho}$ with the B_1 amplitude (ω_1) and a possible off-resonance component ($\Delta\omega_1$). B) The magnetization is flipped into the transverse plane, afterward, a locking field is applied along the y' -axis, to allow for $T_{1\rho}$ relaxation along the effective field. C) The magnetization precesses around the effective field during the spin-lock time (TSL) instead of the main magnetic field for T_1 relaxation. Figure adapted from [24] and [25].

2.2.1. Adiabatic RF Pulses

For several pulse sequences, such as spin echo, inversion recovery, and gradient echo, the \mathbf{B}_1 field has to be applied close to the Larmor frequency. Firstly, to have a larger effective energy transfer, and secondly, to let the net magnetization rotate around the \mathbf{B}_0 field for excitation [1]. Conventionally, these sequences, use RF block pulses with constant amplitude to excite the magnetization and let the magnetization relax afterwards to equilibrium. When the \mathbf{B}_0 or \mathbf{B}_1 field is imperfect, block RF pulses with constant amplitude can cause several problems such as off-resonance artifacts, inaccurate flip angles, and unwanted signal drops. Adiabatic excitation pulses in MR imaging have been proposed to alleviate these limitations. This is because these RF pulses are used to be less sensitive to fluctuations in the RF field and accurately manipulate the magnetization without overheating the sample when field inhomogeneities are present [26]. The idea of adiabatic RF pulses in MR imaging is to make use of RF pulses with off-resonance frequencies regarding the Larmor frequency. Adiabatic RF pulses are performed by sweeping through different frequency ranges and amplitudes of the RF field by using frequency (FM) and amplitude modulated (AM) functions, respectively $\Delta\omega_1(t)$ and $\omega_1(t)$. For instance, a hyperbolic secant (HS) RF pulse with the AM and FM functions (equation 2.9) [26], can be used for an adiabatic inversion or full-passage (AFP). An AFP starts from frequencies far below resonance and goes up to frequencies far above resonance, which is demonstrated in the HS AM and FM functions in figure 2.8.

$$\begin{aligned}\omega_1(t) &= \omega_{max} \operatorname{sech}\left(\beta\left(\frac{2t}{T_p} - 1\right)\right), \\ \Delta\omega_1(t) &= f_{max} \tanh\left(\beta\left(\frac{2t}{T_p} - 1\right)\right).\end{aligned}\quad (2.9)$$

Here β determines the width of the bell shape, T_p is the pulse duration, ω_{max} and f_{max} are the amplitude of the AM and FM functions, respectively. During the presence of the RF pulse, the effective field ($B_{eff}(t)$) is described with [26]:

$$B_{eff}(t) = \sqrt{B_1^2(t) + (\Delta\omega_1(t)/\gamma)^2} = \gamma^{-1} \sqrt{\omega_1^2(t) + \Delta\omega_1^2(t)}. \quad (2.10)$$

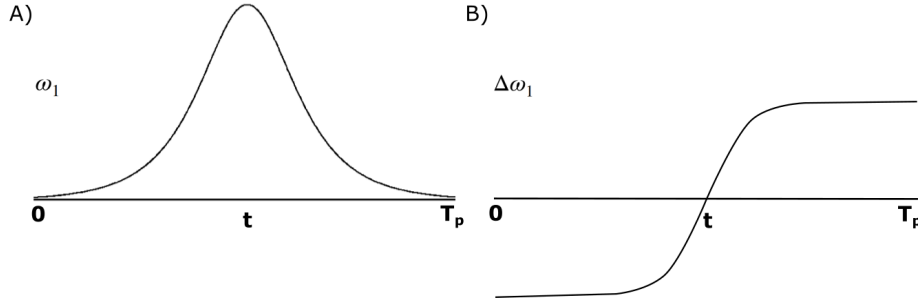


Figure 2.8: A) Amplitude (ω_1) and B) frequency ($\Delta\omega_1$) modulation functions of the hyperbolic secant (HS) pulse. Figure adapted from [26].

The two off-resonance situations and the on-resonance case of the AFP are shown in figure 2.9. For far below resonance, the effective field in the rotating frame starts from being parallel with the main magnetic field ($+z'$). The effective field moves from being anti-parallel ($-z'$) far above resonance. When gradually sweeping through the frequencies, the effective field becomes a locking field, and the magnetization gradually flips along with the effective field (figure 2.9). The locking field directly relates to $T_{1\rho}$ relaxation during excitation. Therefore, adiabatic RF pulses can be used as a preparation pulse for $T_{1\rho}$ contrast. In this kind of preparation pulses, the magnetization is flipped forth and back from and to the original position, and relaxation takes place along the effective which creates a rotating frame relaxation contrast.

As long as the adiabatic condition is satisfied (equation 2.11), the adiabatic RF pulses mechanism allows to manipulate the magnetization accurately when field inhomogeneities are present [26]. However, satisfying the adiabatic conditions still comes at the cost of having a high SAR [1].

$$|B_{eff}(t)| \gg \left| \gamma^{-1} \frac{d\alpha(t)}{dt} \right|, \quad (2.11)$$

where α is the angle between \mathbf{B}_{eff} and $+z'$ -axis (figure 2.9B) and can be calculated in the following way [8]:

$$\alpha(t) = \arctan\left(\frac{\omega_1(t)}{\Delta\omega_1(t)}\right). \quad (2.12)$$

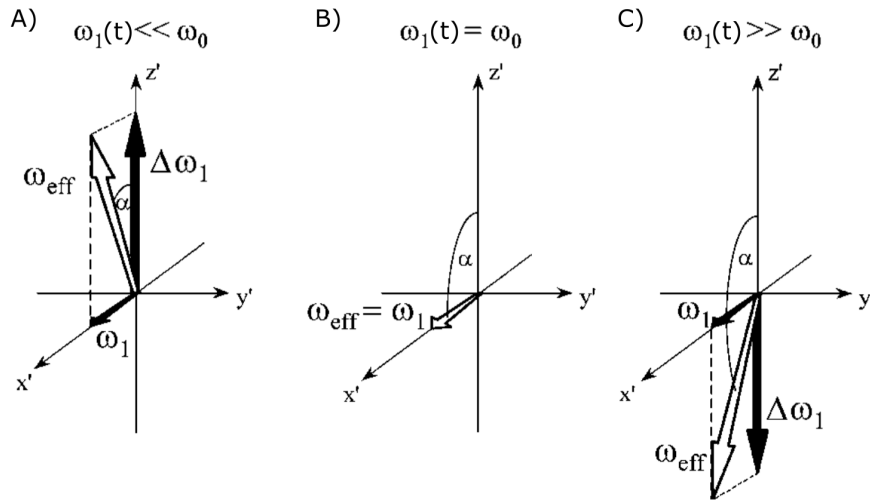


Figure 2.9: The effective field B_{eff} ($= \omega_{eff}/\gamma$) constructed from ω_1 and $\Delta\omega_1$, respectively the \mathbf{B}_1 field and off-resonance component is visualized. As well as, the title angle (α), the angle between ω_{eff} and z' . In the ω_1 frame or the first rotating frame of reference, oscillating at the RF frequency ($\omega_1(t)$). Three situations are shown, A) far below resonance, B) at resonance, and C) far above resonance, where A) and C) are also referred to as off-resonance situations. [26]

2.3. Relaxation Along a Fictitious Field

Besides adiabatic RF pulses, there are RF pulses that operate in the sub-adiabatic regime, which violates the adiabatic condition. Relaxation Along a Fictitious Field, is such an excitation technique that aims to visualize slow molecular motion by using amplitude and frequency modulated functions. It was developed to overcome the SAR limitations of conventional constant amplitude SL and has shown comparable sensitivity to slow molecular motion in tissue [8]. Another advantage of RAFF is the reduced sensitivity to off-resonances compared to conventional SL pulses [8].

Where $T_{1\rho}$ uses a locking field in the first rotating frame to mimic a small energy gap, RAFF does exactly this in the second rotating frame of reference with a constant locking angle ($\epsilon = 45^\circ$) in the second RFR. The second RFR rotates along the tilt angle ($\alpha(t)$), in other words, it is the frame where the z-axis is along $\mathbf{B}_{eff}(t)$, and this direction is denoted by \mathbf{z}'' . Both the first and second RFR are shown in figure 2.10.

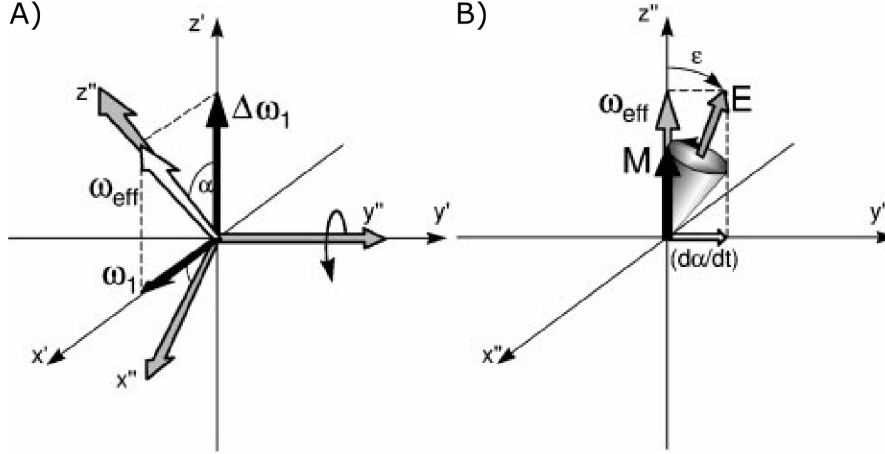


Figure 2.10: Vector diagrams showing the effective field and its components in two rotating frames of reference (RFR). A) Relationship between the ω_1 -frame (1st RFR) and the ω_{eff} -frame (2nd RFR). B) Magnetic field components and evolution of the magnetization vector (M) in the ω_{eff} -frame with E the effective field in the 2nd RFR, $d\alpha/dt$ the fictitious field and ϵ the angle between E and \mathbf{z}'' . Figure adapted from [26]

For the arising fields in the second RFR, an equivalent can be found in the first RFR. When transforming from the laboratory frame to the first rotating frame, the effective field was constructed of two components: the B_1 amplitude and the off-resonance term. An equivalent happens when transforming from the first to the second rotating frame. In this case, the effective in the second RFR ($E(t)$) is composed of $\mathbf{B}_{eff}(t)$ and the fictitious field ($\gamma^{-1} \frac{d\alpha(t)}{dt}$ [T]). The fictitious field arises from the extra rotation of the second RFR. Therefore, $E(t)$ can be written as [8]:

$$E(t) = \sqrt{B_{eff}(t)^2 + \left(\gamma^{-1} \frac{d\alpha(t)}{dt}\right)^2}. \quad (2.13)$$

To overcome the SAR limitations of conventional constant amplitude SL, the AM and FM functions of RAFF are designed to violate the adiabatic condition, but they satisfy the following [8]:

$$|B_{eff}(t)| = \left| \gamma^{-1} \frac{d\alpha(t)}{dt} \right|, \quad (2.14)$$

In this way, the effective and fictitious fields have equal strength, and the change of the effective field rotates exactly one time when the effective field makes one rotation around the main magnetic field. Therefore, the AM and FM functions of RAFF are:

$$\begin{aligned} \omega_1(t) &= \omega_{max} \sin(\omega_{max} t); \\ \Delta\omega_1(t) &= \omega_{max} \cos(\omega_{max} t), \end{aligned} \quad (2.15)$$

with ω_{max} the maximum frequency, determined by the pulse duration:

$$\omega_{max} = \frac{4\pi}{\sqrt{2}T_p}. \quad (2.16)$$

The AM and FM functions in [equation 2.15](#) represent the first quarter (P) of the RF pulse. The total RAFF module ($PP^{-1}P_{\pi}P_{\pi}^{-1}$) is formed using Malcom Levitt (MLEV) phase cycling of a single RAFF segment (P) by alternately reversing the pulse in time and alternately adding no or a π phase jump ([figure 2.11](#)) [8]. The composite pulse's structure is designed to counteract frequency shifts that may arise from factors like variations in magnetic susceptibility within tissues and B_0 inhomogeneities [8]. The frequency shift effects can be rewound by reversing the time of the pulse, resulting in PP^{-1} [8]. Again mirroring, results in $PP^{-1}P_{\pi}P_{\pi}^{-1}$, leading to a balanced pulse around the main magnetic field.

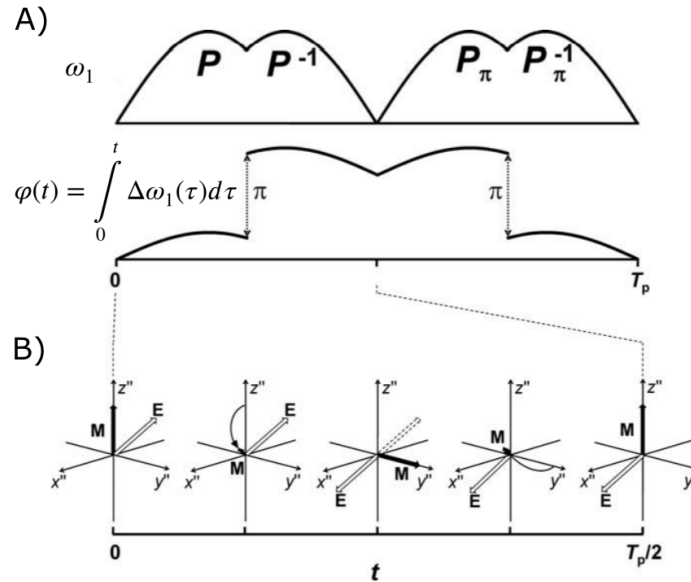


Figure 2.11: A) Amplitude and phase modulations of the RAFF RF pulse divided into quarters (P, P^{-1}, P_{π} and P_{π}^{-1}). The total pulse is constructed as a composite pulse by alternately mirroring the pulse in time and alternately adding no or a π phase jump. B) For half of the RAFF pulse duration ($T_p/2$), the rotation of the magnetization (M) around the effective field (E) is shown in the second rotating frame of reference. [26]

In the end, to use RAFF pulses as a contrast mechanism, the RAFF pulses are used in the preparation phase of a conventional MRI sequence. Before the conventional readout starts, the magnetization is flipped forward and backward from and to the original orientation ([figure 2.11B](#)). During this process, the relaxation along the fictitious field creates the difference in magnetization and a contrast is created for small molecular motion. RAFF has a reduced SAR and is less sensitive to off-resonances compared to conventional SL. The sensitivity to field inhomogeneities remains a limitation of RAFF hampering clinical applications, as field inhomogeneities create imaging artifacts due to the mismatch between the starting and end position [8]. Several RF pulse derivations are shown in [Appendix A](#), which may lead to an RF pulse that outstands the performance of RAFF against field inhomogeneities. The derivation includes RF pulses that are further discussed in the report for a constant effective field ([Appendix A.1](#)).

3

First Findings of Off-resonance and B1+ Resilience of RAFF Pulses

3.1. Introduction

Spin-lock (SL) relaxation times ($T_{1\rho}$) have been proposed as a promising biomarker for multiple diseases, including myocardial fibrosis [7] and cartilage degeneration [9]. However, quantification of $T_{1\rho}$ based on constant amplitude SL pulses implies a high SAR burden and is susceptible to field inhomogeneities. Relaxation Along a Fictitious Field (RAFF) was developed to overcome the SAR limitations of conventional SL (RefSL) [27] and showed comparable sensitivity to slow molecular motion in tissue [8]. Sensitivity to off-resonances is reduced with RAFF, but remains a limitation. This hinders quantification quality and hampers clinical applications. In this work, the susceptibility of RAFF pulses to field inhomogeneities is investigated and an improved pulse for fictitious field SL relaxometry with increased resilience against off-resonance and B_1^+ inhomogeneities is proposed.

3.2. Methods

The performances of RefSL, RAFF, and yet another RAFF (yaRAFF) pulses are investigated using Bloch simulations and phantom acquisitions for varying B_0 and B_1^+ inhomogeneities. For yaRAFF, as opposed to RAFF, the fictitious field strength is decoupled from the effective field strength, leading to an RF shape with a weighted sum of sine and cosine (figure 3.1C). Bloch simulations were used to find optimal weighting parameter β and ω_{max} values for yaRAFF (figure 3.2). Different measures were used to quantify pulse performance in the optimization: 1) The averaged preparation efficiency M_z/M_0 over the region of interest (ROI) $(\eta_1, \Delta\omega_1) \in [0.5, 1] \times [-200, 200]$ Hz, here η_1 is the ratio between effective and nominal B_1^+ power and $\Delta\omega_1$ the off-resonance frequency. 2) The magnetization path length as a measure of spin-locking efficiency (figure 3.2B-C). In phantom validation experiments were conducted for $\eta_1 = [0.2, 0.4, \dots, 1]$ with $\Delta\omega_1 = [-200, -180, \dots, 200]$ Hz for RefSL, and $\Delta\omega_1 = [-400, -380, \dots, 400]$ Hz for RAFF and yaRAFF (figure 3.3). The FWHM was defined as the frequency width at $M_z/M_0 = 0.5$. For mapping quality assessment, in vivo T_{RAFF} maps of the calf were acquired at nine off-resonances ($\Delta\omega_1 = [-200, -150, \dots, 200]$ Hz) in two healthy subjects (1 male and 1 female, 26 ± 1 y, figure 3.4, 3.5).

Mapping was performed at 3T (Philips Ingenia) acquiring 4 T_{RAFF} -prepared bSSFP images (max RF power = 13.5 μ T, pulse duration = 2.84 ms, preparation duration = 0, 28, 57, 85 ms) and a saturation image to compensate for the effects of the imaging readout (figure 3.1A) [28]. All scans shared the following imaging parameters: resolution = 2×2 mm², slice-thickness = 8 mm, FOV = 181x181 mm², flip-angle = 70°, TE/TR = 0.83/2.05 ms. Quantitative maps were obtained by fitting a three-parameter model. The coefficient of variation (CoV) within manually-drawn ROIs was used to assess precision (figure 3.5).

3.3. Results

Simulation results show an increase in averaged M_z for increasing peak frequency with the yaRAFF-pulse (figure 3.2A). At 500 Hz (maximum allowed frequency), the averaged M_z showed an increasing trend for smaller β , while the magnetization path length decreased. The optimal $\beta = 0.62$ resulted in higher performance

(0.973) compared with RAFF (0.919) (figure 3.2B). In simulations, the FWHM of the off-resonance response was 320 ± 8 , 448 ± 8 , and 668 ± 8 Hz, for RefSL, RAFF, and yaRAFF, respectively. Phantom experiments show close agreement with the simulations (figure 3.3), yielding an off-resonance FWHM of 240 ± 20 , 500 ± 25 , and 700 ± 50 Hz for RefSL, RAFF, and yaRAFF, respectively. In-vivo magnitude baseline images acquired in one healthy subject are shown in figure 3.4 for RefSL, RAFF, and yaRAFF at nine off-resonances ($\Delta\omega_1 = \pm 200$ Hz). RefSL shows poor resilience against off-resonance artifacts (figure 3.4A). Across several off-resonances yaRAFF achieves more homogeneous signal intensities compared with RAFF (figure 3.4B-C). For quantitative mapping, RefSL shows poor precision in the presence of off-resonances with a CoV > 15%, while RAFF and yaRAFF yield substantially improved off-resonance resilience, with an average CoV of 3.1% and 2.9% for $|\Delta\omega_1| < 200$ Hz, respectively (figure 3.5).

3.4. Discussion

In this work, we investigate the susceptibility of fictitious field spin-lock pulses against field inhomogeneities. Simulations and phantom experiments show good resilience against B_1^+ inhomogeneities but moderate susceptibility to off-resonance. An adapted pulse, yaRAFF, is proposed to improve off-resonance sensitivity. Phantom and in vivo results show 40% and 191% increased off-resonance tolerance with yaRAFF compared to RAFF and constant-amplitude spin-lock, respectively. RAFF pulses operate in a sub-adiabatic regime, where the effective field strength and fictitious field strength are matched. yaRAFF is based on relaxing this condition to yield an amplitude and frequency-modulated pulse, which operates closer to the adiabatic conditions. Resulting in, increased off-resonance performance, while maintaining a spin-lock at an effective field with comparable strength. The implemented yaRAFF had an alternation in the frequency modulation function, leading to a slight off-center frequency shift. Thus, increased resilience against positive off-resonance compared with negative off-resonance is observed. Consequently, for in vivo application, the pulse is best played at a positive off-resonance shift, to center the off-resonance tolerance around 0. Image quality, as well as the precision of quantitative spin-lock mapping, obtained with the RefSL, RAFF and yaRAFF pulses showed strong susceptibility to off-resonances. yaRAFF achieved the largest resilience, to off-resonances in vivo, and the best precision in quantitative measurements. Consequently, yaRAFF may offer a promising alternative for sensitization to slow molecular motion, where high resilience against off-resonance is required.

3.5. Conclusion

In simulations and phantom experiments, RAFF pulses show good resilience against B_1^+ inhomogeneities and moderate resilience against B_0 inhomogeneities. Decoupling the effective field strength from the fictitious field strength in yaRAFF helps to further improve off-resonance resilience, leading to a 40% increase in off-resonance tolerance with a maintained consistency of in vivo precision in the calf at 3T.

3.6. Figures

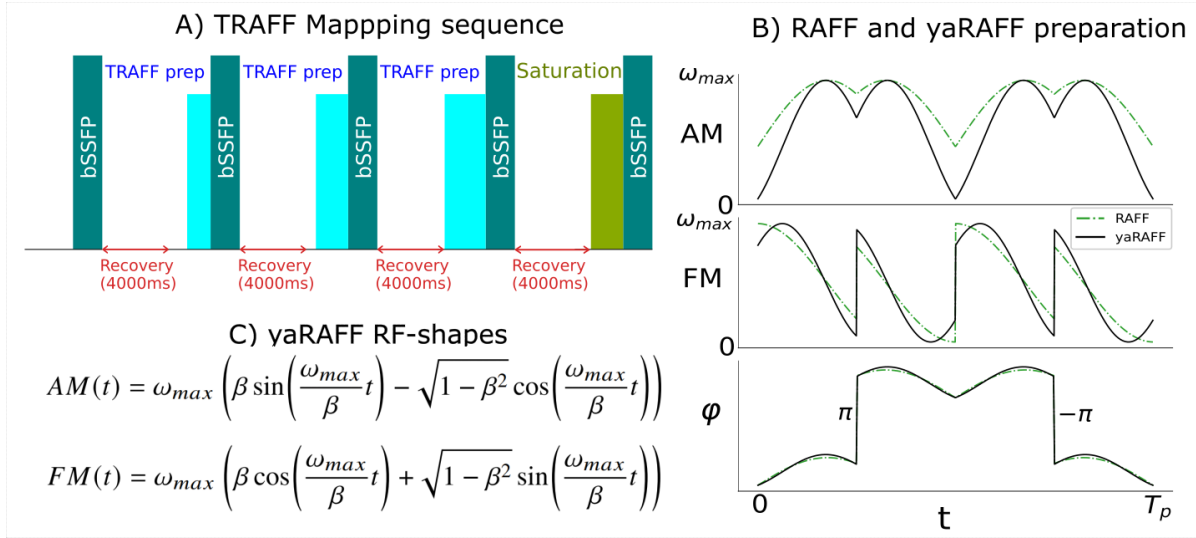


Figure 3.1: A) Schematic representation of the T_{RAFF} mapping sequence for four T_{RAFF} -prepared images (0, 28, 57, 85 ms) and one saturation image with a 4s recovery in between acquisitions. Other acquisition parameters were: resolution = $2 \times 2 \times 8 \text{ mm}^3$, FOV = $181 \times 181 \times 8 \text{ mm}^3$, and the bSSFP readout with a 70° flip-angle and TE/TR = 0.83/2.05 ms. B) Radiofrequency shapes: amplitude modulation, frequency modulation, and phase for both RAFF and yaRAFF. C) Corresponding yaRAFF RF-shapes equation.

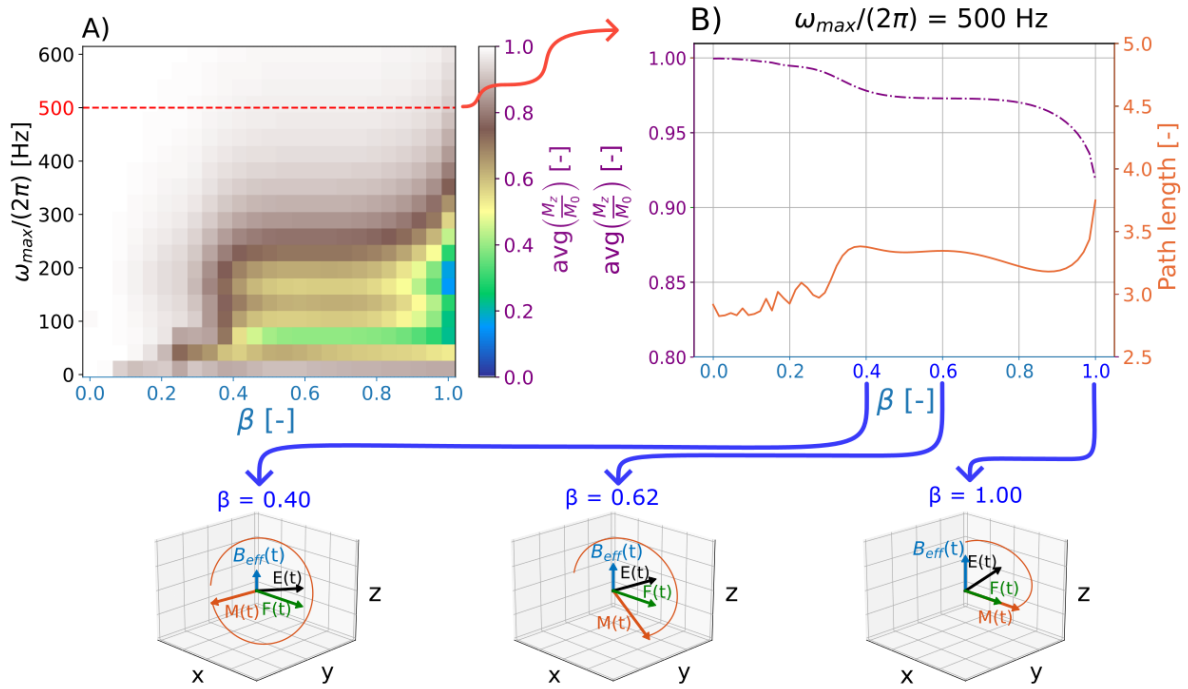


Figure 3.2: A) yaRAFF simulated optimization for the shape parameter, β , and peak frequency for M_z/M_0 with the averaged domain $(\eta_1, \Delta\omega_1) \in [0.5, 1] \times [-200, 200]$ Hz. B) Single frequency (500 Hz) yaRAFF optimization, considering the magnetization path length as a measure of spin-locking efficiency. Bottom row: Magnetization behavior at several β s, indicating the magnetization vector $M(t)$, red, with its trajectory, effective field B_{eff} , blue, fictitious field $F(t)$, green, and resulting field $E(t)$, black shown in the B_{eff} rotating frame. The optimal shape parameter was determined as $\beta = 0.62$.

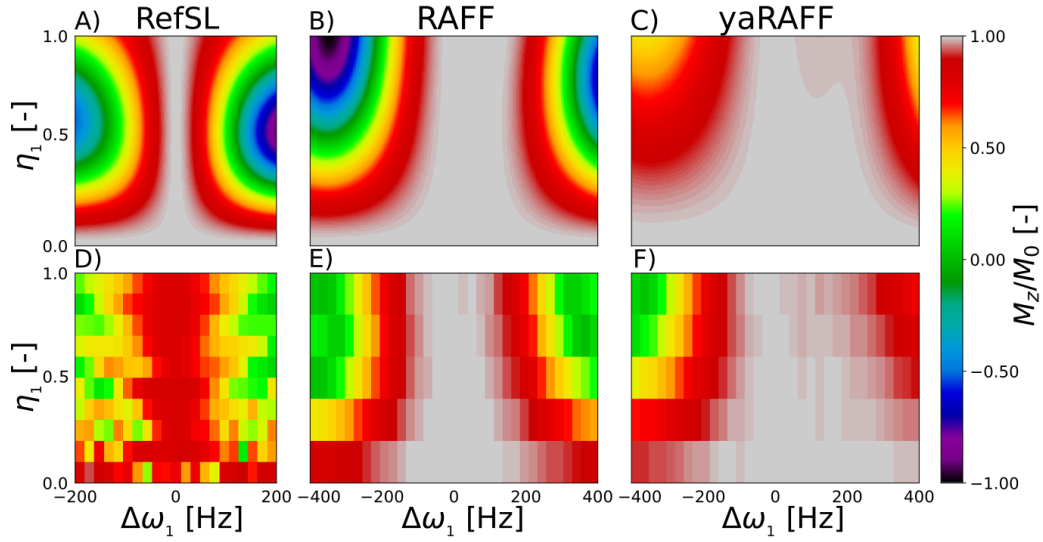


Figure 3.3: Performance maps for relative B_0 and B_1^+ artifacts of M_z/M_0 obtained in simulations (A, B, C) and phantom (D, E, F) for RefSL (A, D), RAFF (B, E), and yaRAFF (C, F), respectively. Here η_1 is the ratio between the effective and nominal B^+1 power. In simulations FWHM of 320 ± 8 , 448 ± 8 , and 668 ± 8 Hz, was measured for RefSL, RAFF and yaRAFF, respectively. In phantom with a single RefSL, RAFF and yaRAFF preparation of 2.8 ms and 500 Hz peak frequency FWHM of 240 ± 20 , 500 ± 25 and 700 ± 50 Hz was obtained.

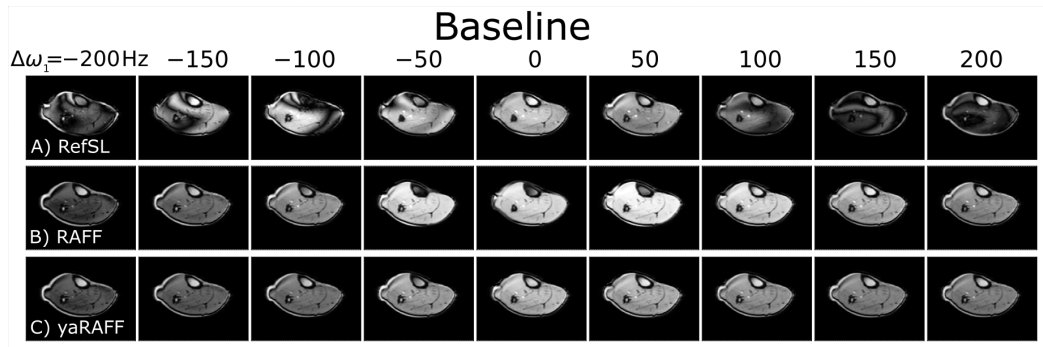


Figure 3.4: In vivo baseline magnitude images of the calf at nine off-resonance frequencies $\Delta\omega_1 = [-200, -180, \dots, 200]$ Hz. baseline images of RefSL (A), RAFF (B) and yaRAFF (C) with a preparation pulse of 28 ms and peak frequency of 500 Hz.

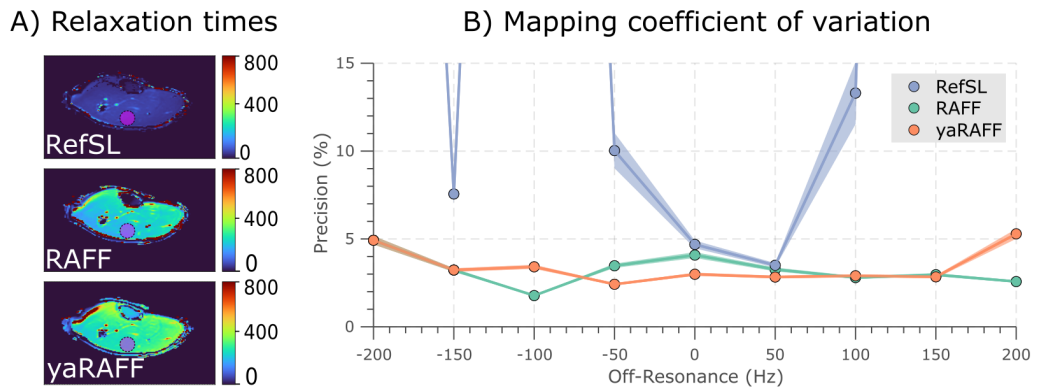


Figure 3.5: A) $T_{1\rho}$, T_{RAFF} and T_{yaRAFF} maps, of one healthy volunteer acquired on-resonance. A circular region of interest (ROI) with muscle tissue was selected. B) The coefficient of variation of the RefSL, RAFF and yaRAFF mappings acquired in the calf of two volunteers at nine off-resonance frequencies $\Delta\omega_1 = [-200, -180, \dots, 200]$ Hz. The average was taken over the ROI and the two volunteers for the coefficient of variation precision measure.

4

Final Findings of Off-resonance and B_1^+ Resilience of RAFF Pulses

4.1. Introduction

Quantitative Magnetic Resonance Imaging (qMRI) is increasingly gaining attention for its ability to early diagnosis and staging of a plethora of diseases across numerous anatomies [9, 10, 19, 7]. Conventional Magnetic Resonance Imaging (MRI) relaxation times, such as T_1 and T_2 , have been most widely used. Rotating frame relaxation times, such as longitudinal relaxation in a rotating frame of reference (RFR), also known as $T_{1\rho}$, have also been proposed with a potentially higher sensitivity to slow molecular motion than T_1 [9]. $T_{1\rho}$ describes the relaxation time measured during radiofrequency (RF) irradiation through spin-lock (SL) pulses. The $T_{1\rho}$ contrast is influenced by several possible processes that play a role, like dipolar interactions, chemical exchange, and diffusion effects [25]. These interactions are typically in the Hz to kHz range, whereas processes for T_1 relaxation are in the kHz to MHz range [25, 24].

Quantification of the $T_{1\rho}$ times, has proven to be particularly promising for the assessment of cartilage degeneration, for example in the context of osteoarthritis [20, 6, 29]. However, conventional spin-lattice relaxation in the rotating frame, $T_{1\rho}$, has the downside of having a high specific absorption rate (SAR) burden and showing high susceptibility to field inhomogeneities [7], which hinders its usage in clinical practice. Improved resilience against field inhomogeneities can be achieved with adiabatic $T_{1\rho}$ [26]. However, the adiabatic pulses in adiabatic $T_{1\rho}$ commonly exhibit a non-constant effective and fictitious field, leading to differences in sensitivity compared with conventional spin-lock pulses.

Relaxation Along a Fictitious Field (RAFF) was proposed to overcome the SAR limitations of conventional constant amplitude SL (RefSL) [27] and showed comparable sensitivity to slow molecular motion in tissue [8]. RAFF was designed to be sensitive to slow molecular motion by using amplitude (AM) and frequency modulated (FM) functions which operate in the sub-adiabatic regime [8]. During the presence of the RAFF RF pulse, the behavior of the magnetic field can be described in a double rotating frame of reference [26]. RAFF generalizes spin-locking for higher-order rotating frames, where $T_{1\rho}$ does in the first RFR. Currently, RAFF is susceptible to B_0 and B_1^+ inhomogeneities [11], which can impair relaxation mapping. As a result, it hinders robust quantification and its wide use in the clinic.

In this work, we sought to investigate the resilience of RAFF pulses against B_0 and B_1^+ field inhomogeneities at 3T. A parametric formulation of the conventional RAFF pulse, so-called parametric RAFF (pRAFF) is also introduced, to enable tailored off-resonance and B_1^+ resilience. pRAFF is optimized using Bloch simulations, and phantom and in vivo calf images of healthy subjects were acquired to compare the performances of conventional RAFF and optimized pRAFF preparations in the presence of field inhomogeneities. Quantitative mapping quality and robustness to system imperfections were compared for RAFF and pRAFF pulses in the knee cartilage. Finally, the reproducibility of RAFF and pRAFF was assessed in the calf of 3 healthy subjects.

4.2. Methods

4.2.1. RF Pulse Design

RAFF pulses are designed to achieve equal fictitious $\left(F(t) = \gamma^{-1} \frac{d\alpha(t)}{dt}\right)$ and effective magnetic field $(B_{eff}(t))$ strength, by respecting the following condition [8]:

$$B_{eff}(t) = \gamma^{-1} \frac{d\alpha(t)}{dt}, \quad (4.1)$$

leading to higher order spin-lock, where the effective and fictitious field compose the locking field $(E(t))$ with a locking angle $(\varepsilon(t))$ of 45° in the second RFR (figure 4.1D). As a result, the amplitude $(\omega_1(t))$ and frequency modulation $(\Delta\omega_1(t))$ function of RAFF pulses can be written as:

$$\omega_1(t) = \omega_{max} \sin(\omega_{max} t); \quad (4.2)$$

$$\Delta\omega_1(t) = \omega_{max} \cos(\omega_{max} t), \quad (4.3)$$

with ω_{max} the maximum frequency, determined by the pulse duration

$$\omega_{max} = \frac{4\pi}{\sqrt{2}T_{p,RAFF}}. \quad (4.4)$$

Equations (4.2) and (4.3) can be generalized with 3 degrees of freedom (DoF), ν, θ, ρ , while maintaining a constant effective field strength, to yield parametric RAFF (pRAFF) amplitude and frequency modulation functions:

$$\omega_1(t) = \omega_{max} \sin\left(\frac{\omega_{max}}{\nu} t - \theta\right), \quad (4.5)$$

$$\Delta\omega_1(t) = \omega_{max} \cos\left(\frac{\omega_{max}}{\nu} t - \theta\right). \quad (4.6)$$

Here ν determines the ratio of the fictitious and effective field strength and thereby affects the locking angle, $\varepsilon(t)$. Thus $\nu = 1$, yields the conventional RAFF pulse, while large ν satisfies the adiabatic condition (Equation (4.7)) and disentangles equal field strengths.

$$\nu = \frac{B_{eff}(t)}{\gamma^{-1} \frac{d\alpha(t)}{dt}}. \quad (4.7)$$

θ indicates the starting angle of the effective field of the RF pulse with respect to the z-axis of the first RFR, denoted with z' -axis. Finally, ρ is the coefficient determining the pRAFF pulse duration $(T_{p,pRAFF})$ by scaling the original RAFF pulse duration $(T_{p,RAFF})$, which determines the spin-lock time. The original RAFF pulse is obtained for the parameter combination $\theta = 0$ rad, $\nu = 1$, and $\rho = 1$, and the total (p)RAFF module is formed using Malcom Levitt (MLEV) phase cycling of a single (p)RAFF segment, where every other segment is time-reversed [8] (figure 4.1B).

During the presence of the pRAFF RF pulse, the parameterized influence on the magnetization can be illustrated by using a double-rotating frame of reference (supplementary figure 4.6-4.8). The first RFR is oscillating at the RF pulse frequency $(\omega_1(t))$. In the second RFR, $B_{eff}(t)$ is aligned with the z' -axis (figure 4.1D). In a similar fashion, RAFF and pRAFF field components, which are extensively described in the supporting information, can be visualized in a double-rotating RFR (figure 4.1D & E), along with the resulting magnetization trajectories and two off-resonances conditions in figure 4.1F & G.

Bloch Simulations

The pulse performance of different pRAFF pulses for varying design parameters θ , ν , ρ , and ω_{max} was investigated using Bloch simulations, implemented in Python 3.6 [30]. Two metrics were used to quantify the pulse performance

1. The averaged preparation efficiency $M_z(T_p)/M_0$ over the design region across a range of B_0 and B_1^+ inhomogeneities.
2. The magnetization path length throughout the pulse as a measure of spin-locking effects, avoiding pulse inefficacy.

Off-resonances $\Delta\omega_1^{off}$ were considered across the range $[-400, 400]$ Hz. B_1^+ inhomogeneities were considered with a scaling factor η_1 , as the ratio of the effective and nominal B_1^+ with $\eta_1 \in [0.5, 1]$. All simulations were limited by the peak B_1^+ power ($B_1^{\max} = 13.5 \mu\text{T}$) and a whole body SAR < 2.0 W/kg.

pRAFF pulses were evaluated across the parameter space with $(\theta, \nu, \rho) \in [0, \pi] \text{ rad} \times [0.1, 10] \times [0.1, 10]$. For all pulses across the parameter space the strength of the effective field is fixed, irrespective of pulse duration. The peak amplitude, ω_{max} , was fixed to 500 Hz, in line with commonly used spin-locking amplitudes at 3T [24], resulting in $T_{p,RAFF} = 2.83$ ms. The parameter combination θ, ν and ρ resulting in the best pulse performance was selected as the optimal pRAFF design for further investigation.

Imaging

All imaging was performed at 3T scanner (Ingenia, Philips, Best, The Netherlands).

The pulse preparation efficiency, $M_z(T_p)/M_0$, was computed as the ratio of two balanced steady-state free-precession (bSSFP) images. One image was acquired with and one without preparation using the respective pulse followed by gradient spoiling to prepare the longitudinal magnetization. A 4 s gap between the two scans was applied to allow for longitudinal magnetization recovery. During post-processing, the signal polarity was extracted from the corresponding phase images. The low-resolution bSSFP images were obtained with the following imaging parameters: resolution = $2 \times 2 \text{ mm}^2$, slice-thickness = 8 mm, FOV = $204 \times 204 \text{ mm}^2$, flip-angle = 70° , TE/TR = 1.37/2.7 ms and a SENSE factor of 2.

In phantom, the calf, and the knee cartilage, relaxation time mapping was acquired with 4 (p)RAFF-prepared spoiled gradient echo (spGRE) images (RAFF single pulse duration = 2.83 ms, preparation duration = 0, 28, 57 and 85 ms) and a saturation image to capture the effect of the imaging readout [31] (figure 4.1A). Identical (p)RAFF pulses, were repeated multiple times to obtain the total preparation duration. Between each repetition, a spoiling gradient was applied to suppress stimulated echos and aggravating excitation by off-resonance effects. After each readout, a 3 s gap was applied to allow for longitudinal magnetization recovery. All scans shared the following imaging parameters: resolution = $0.8 \times 0.8 \text{ mm}^2$, slice-thickness = 3 mm, FOV = $181 \times 181 \text{ mm}^2$, flip-angle = 15° , number of shots = 6, and a SENSE factor of 2. The TE/TR varied between experiments, resulting in phantom studies TE/TR = 2.5/7.9 ms, calf TE/TR = 2.4/7.8 ms, and knee cartilage TE/TR = 1.94/6.7 ms.

Relaxation times maps were obtained by fitting the following three-parameter model [31] with MATLAB R2021b (MathWorks, Natick, USA), to account for the readout effect of the imaging pulses:

$$S(t) = A \cdot e^{-\frac{t}{T_{(p)RAFF}}} + B. \quad (4.8)$$

Parametric Study

The effect of design parameter changes in (p)RAFF was studied in phantom (TIMES [32]) and the calf muscle of four healthy subjects (3 males and 1 female, 26 ± 2 y.o.). T_{pRAFF} maps were acquired by independently varying each parameter while keeping the remaining two parameters fixed at the original RAFF value ($\theta = 0$ rad, $\nu = 1$ and $\rho = 1$). The following values were tested for each parameter: $\theta = [0, 0.1\pi, \dots, \pi]$ rad, $\nu = [0.1, 1, 2, 3, \dots, 10]$ and $\rho = [1, 2, 3, \dots, 10]$. Moreover, maps were acquired for $\{\rho, \nu\}$ such as $\rho = \nu\sqrt{2}$ for $\nu = [1, 1.75, 2.5, \dots, 7]$, corresponding to the 1-DoF space where the optimal pRAFF solution is found. Examples of the corresponding RF shapes and magnetization trajectory are visualized in supplementary figure 4.6-4.9. Relaxation times were evaluated in circular ROIs manually drawn within the individual phantom vial most closely resembling muscle tissue and the calf muscle, respectively.

B_0 and B_1^+ Inhomogeneities Resilience Study

Simulation results were validated with phantom experiments on a bottle phantom (Spectrasyn 4 polyal-phaolefin, ExxonMobil Chemical). The preparation efficiency of the RAFF and the optimized pRAFF pulse, was tested by modifying the offset frequency $\Delta\omega_1^{off} \in [-400, -375, \dots, 400]$ Hz and scaling the pulse amplitude by $\eta_1 \in [0.05, 0.1, \dots, 1.0]$ for each frequency value.

Firstly, the effect of off-resonance and B_1^+ inhomogeneity on the mapping performance was investigated in isolation. To this end, acquisitions were performed in the TIMES phantom and in 3 healthy subjects (2 males and 1 female, 24 ± 3 y.o.). For each pulse, maps were acquired at 13 off-resonance frequencies $\Delta\omega_1^{off} = [-300, -250, \dots, 300]$ Hz in a first experiment and for 10 relative B_1^+ inhomogeneities $\eta_1 = [0.1, 0.2, \dots, 1]$ in a second experiment. The consistency performance of both pulses against individual B_0 and B_1^+ inhomogeneities are quantified by specifying the range where the relaxation time stays $\pm 10\%$ of the on-resonance case.

Next, mapping performance was obtained for a combination of B_0 and B_1^+ field inhomogeneities: $\Delta\omega_1^{off} = [-150, 0, 150]$ Hz for each $\eta_1 = [0.5, 0.75, 1.0]$. For each pulse, 9 maps were obtained in the TIMES phantom, in the calf of one healthy subject (1 male, 28 y.o.), and in the knee cartilage of one healthy subject (1 male, 27 y.o.). Mapping quality and relaxation times of knee cartilage were assessed in manually drawn ROIs containing the cartilage. The coefficient of variation (CoV) within field inhomogeneities was used to quantify variability. The CoV was computed as the ratio between the standard deviation (std) across field inhomogeneities and the mean relaxation time of the ROIs.

Finally, mapping repeatability was assessed for 6 of the 9 maps of the combined field inhomogeneities, 3 maps with $\eta_1 = 1$ for $\Delta\omega_1^{off} = [-150, 0, 150]$ Hz and $\Delta\omega_1^{off} = 0$ Hz for $\eta_1 = [0.5, 0.75, 1]$, were obtained in the calf in 3 healthy subjects (3 male, 26 ± 2 y.o.).

4.3. Results

4.3.1. Bloch Simulations Results

figure 4.2A shows a visualization of the pulse performance across the 3D parameter space. The 2D planes intersecting with the original RAFF pulse parameters ($\theta = 0$ rad, $\nu = 1$ and $\rho = 1$) are depicted in figure 4.2B & C in terms of preparation efficiency and magnetization path length. All cross-sections indicated an increased averaged M_z for small preparation duration factors ρ and small values of ν . Simultaneously, however, the magnetization path length drops substantially for small ρ and ν , indicating no effective spin-locking behavior caused by reduced effective field amplitudes.

A pattern of high preparation efficiency and path length is observed for $\rho = \sqrt{2}\nu$ (figure 4.2B-C, middle). Improved performance is shown for higher harmonics ($\rho = \sqrt{2}^n \nu$, $n = 2, 3, \dots$) as well. The optimal combination of parameters for pRAFF was found for $\theta = 0$ rad, $\nu = 5.53$ and $\rho = 7.82$, also satisfying $\rho = \sqrt{2}\nu$.

Parametric Results

The parametric change of θ (figure 4.2D) shows a cyclic behavior with maximal values around $\theta \approx \pi/4$ and minimal values around $\theta \approx 3\pi/4$ both in the phantom and in vivo. Changes in ρ led to only minor alteration in T_{pRAFF} , except for $\rho = 1$ (figure 4.2E). For the parametric change of ν , increasing relaxation times are obtained for increased adiabaticity both in the phantom and calf, except for $\nu = 0.1$ (figure 4.2F). Finally, the parametric change along the line $\rho = \nu\sqrt{2}$, in figure 4.2G, shows only minor changes in T_{pRAFF} for increasing ρ and ν .

4.3.2. B_0 and B_1^+ Inhomogeneities Resilience Results

Phantom and Calf Field Inhomogeneities Resilience Results

figure 4.3A-D shows the performance maps for $(\eta_1, \Delta\omega_1^{off}) \in [0, 1] \times [-400, 400]$ Hz in simulations and phantom. In simulations, it is apparent that pRAFF has an increased off-resonance bandwidth yielding a larger homogeneous pulse performance compared with RAFF. The average pulse performance across the design region for these parameters was 0.95 compared with 0.36 for RAFF (figure 4.2B). These results were well reproduced in phantom experiments, which yielded an averaged M_z of 0.67 and 0.91 for RAFF and pRAFF, respectively, over the design region (figure 4.3C & D). At the same, when considering the design region in figure 4.3A & C, RAFF shows an off-resonance bandwidth of 300 ± 25 Hz for a 10% tolerance. On the contrary, pRAFF cannot be described with one bandwidth for the entire design region, but the minimum bandwidth is in the order of 500 Hz. In visual inspection, the simulated RAFF and phantom performance show the same shape hyperbolic shape and comparable center region size. For pRAFF, a similar shape observation can be made. The location of the low-resolution speckle structure in the outer plane agrees between simulation and phantom performance.

In figure 4.3E & F, phantom maps for several B_0 and B_1^+ inhomogeneities are shown, at on-resonance the relaxation times were measured as $T_{RAFF} = 98 \pm 3$ ms and $T_{pRAFF} = 74 \pm 2$ ms. Consistent mapping quality is shown for pRAFF across the studied range of B_0 and B_1^+ inhomogeneities, with visually only minor differences between the off-resonance and η_1 values. RAFF, on the other hand, shows large T_{RAFF} fluctuations for all field inhomogeneities. Similar results for the field inhomogeneities are shown in the calf muscle $T_{(p)RAFF}$ maps (supplementary figure 4.10C & D) and the averaged relaxation time of each selected ROI (supplementary figure 4.10A & B), with $T_{RAFF} = 34 \pm 1$ ms and $T_{pRAFF} = 50 \pm 1$ ms at on-resonance. Across all field inhomogeneities, RAFF has a CoV of 78.2% and 78.3% in the phantom and calf whereas pRAFF shows increased consistency with a CoV of 11% and 6.5% in the phantom and calf, respectively.

For phantom and in vivo calf mapping, on-resonance maps with the manually drawn ROIs containing a vial or muscle tissue are shown respectively in figure 4.4A & B. figure 4.4, shows the field inhomogeneities performances of RAFF and pRAFF. For both, the calf and phantom, T_{pRAFF} shows less than $\pm 10\%$ deviation over a large range of off-resonances (figure 4.4C & D), while T_{RAFF} times are marked with large deviations in the presence of smaller off-resonances. In the phantom, the frequency width with less than $\pm 10\%$ deviation was 447 ± 31 Hz for pRAFF compared with 74 ± 23 Hz for RAFF. In vivo, similar ranges were obtained, with a frequency width of 496 ± 14 Hz for pRAFF compared with 104 ± 8 Hz for RAFF. For both pulses, a 50 Hz shift of the center frequency is visible. For relative B_1^+ performance, RAFF exhibits increased relaxation times at decreased effective B_1^+ and exceeds the $\pm 10\%$ bound for $0.9 < \eta_1$. On the contrary, pRAFF remains within the tolerance for a large range, $0.5 \leq \eta_1 \leq 1$ and $0.4 \leq \eta_1 \leq 1$, respectively in the phantom and calf. Outside the tolerance, pRAFF shows diverse behavior, decreasing and increasing T_{pRAFF} in figure 4.4E & F for respectively the phantom and calf.

In Vivo Knee Cartilage Field Inhomogeneities Resilience Results

RAFF and pRAFF-based relaxation maps, acquired on-resonance are depicted in figure 4.5B & C. Relaxation times of 42 ± 11 ms (RAFF) compared to 50 ± 14 ms (pRAFF) were found in the knee cartilage on-resonance. In figure 4.5E & F, shows an overlap of the cartilage quantification at various B_0 and B_1^+ inhomogeneities with the none RF prepared baseline images. pRAFF shows consistent mapping results for all field inhomogeneities. On the contrary, RAFF shows large fluctuations for all field inhomogeneities. Compared with on-resonance, T_{RAFF} times are enlarged for decreasing field strength and are impaired for increasing off-resonances. Across all field inhomogeneities a CoV of 57% was observed for RAFF versus 11% for pRAFF (figure 4.5A & C). In the reproducibility assessment for the robustness of RAFF and pRAFF against field inhomogeneities, standard deviations of 4%. and 3%. were found for the CoV across subjects, respectively.

4.4. Discussion

In this work, the resilience of RAFF pulses against field inhomogeneities is investigated. Phantom experiments show strong susceptibility to changes in the B_1^+ field but moderate resilience against off-resonances for RAFF. Parameterization of the RAFF formulation allowed to derive pulses that maintain constant effective and fictitious fields. The optimized, parameterized pulse, pRAFF obtained shows 440% increased off-resonance resilience and 450% increased resilience against B_1^+ inhomogeneity while maintaining mapping quality and contrast in the phantom, calf, and knee cartilage.

In conventional MRI, the sensitivity to slow molecular motion can be obtained at the cost of losing signal-to-noise ratio (SNR). The advantage of rotating frame relaxation is its sensitivity to slow molecular motion at all field strengths without the loss of SNR. The RAFF pulse generalizes spin-locking for higher-order rotating frames and operates in a sub-adiabatic regime, where the effective field strength and fictitious field strength are matched. The parameterization in Equation (4.5) is based on relaxing this condition to yield an amplitude and frequency-modulated pulse, which can operate closer to or further away from the adiabatic conditions. The optimized pRAFF moves closer to the adiabatic condition. The presence of a relatively stronger locking field results in changes in the preparation sensitivity to different molecular and intra-molecular effects. Consequently, figure 4.5B & C showed increased relaxation times in the muscle, fat and knee cartilage for pRAFF compared with RAFF. Comparable RAFF relaxation times were found in a few studies with higher peak frequencies in humans [19] and horses [6]. On the other hand, increased and impaired T_{RAFF} values were, respectively, found in a bovine [33], and rabbit model [29]. Detailed investigation of the potential or loss of sensitivity as biomarker with parameterized RAFF is warranted.

Phantom and in vivo calf off-resonance mapping experiments (figure 4.4C & D) showed increased resilience against field inhomogeneities for pRAFF with respect to RAFF. Compared to the single pulse experiments, an overall decreased bandwidth is observed in mapping with either pulse, due to the accumulating effect of the repeated pulse application (figure 4.4C & D). Accordingly, preparation duration leads to a trade-off between preparation efficiency and fit conditioning in the quantification. The pRAFF module is 7.82 times longer than RAFF (figure 4.1), thus, requiring fewer repetitions to achieve the same preparation duration. Relative to the in-vivo relaxation time ($T_{RAFF} = 34 \pm 1$ ms versus $T_{pRAFF} = 50 \pm 1$ ms), effectively 5.32 times fewer repetitions are needed for comparable fit conditioning. As a result, phantom and calf mapping of pRAFF (figure 4.4C & D) closely resemble the preparation efficiency in the simulation and phantom (figure 4.3B & D).

High efficiency was observed for pulses with minimal path length, such as those with very low ν . How-

ever, for these pulses very little relaxation is induced, hampering sensitivity and potential quantification. This effect is visible in the mapping results, where low ν values yield largely increased relaxation times, with relatively large uncertainty (figure 4.2F). Thus, the magnetization path length was considered an essential marker to ensure pulse effectiveness and to differentiate between actual and fictitiously high efficiencies.

Considering the different relaxation time behaviors, the specific tissue and RF pulse interaction may differ greatly. However, pRAFF shows hardly any fluctuations in relaxation times for all obtained field inhomogeneities (figure 4.5E & F) with 5 times reduced CoV for pRAFF compared to RAFF. Furthermore, minimal differences in the CoV was found across subjects for combined field inhomogeneities. Thus, conforming simulation and phantom results, increased off-resonance performance is achieved while maintaining a spin-lock with the same effective strength field. Consequently, pRAFF may offer a promising alternative for sensitization to slow molecular motion, where high resilience against off-resonance is required.

The optimal performance and improved resilience against field inhomogeneities were found to move from the sub-adiabatic to a near adiabatic regime. Even though the RAFF field inhomogeneity resilience is increased for pRAFF, its sensitivity to tissue types has been changed, as shown in the knee on-resonance maps (figure 4.5B & C). In a similar fashion, its function as biomarker for certain diseases is possibly adapted, which could mean the loss of sensitivity to osteoarthritis or other pathological remodeling. At the same time, potential complementary or redundant information with respect to RAFF and conventional relaxation times T_1 and T_2 , or sensitivity to different pathological processes may be attained. Thus, clinical studies are needed in further research to validate pRAFF in different pathologies. Patients with osteoarthritis are of particular interest, due to the established value of spin-lock imaging biomarkers. However, other clinical applications of spin-lock relaxometry, such as non-contrast assessment of myocardial scar, also bear great promise due to the larger off-resonance resilience. Clinical studies in relevant patient cohorts, as well as reproducibility across scanners, is ultimately warranted to determine the potential value of pRAFF as a prospective quantitative imaging biomarker.

4.5. Conclusions

In this work, RAFF pulses on a clinical 3T system were shown to demonstrate moderate resilience against off-resonances but strong susceptibility to B_1^+ inhomogeneities. A parameterized RAFF (pRAFF) formulation allowed for the derivation of preparation pulses with constant effective and fictitious fields with improved resilience against field inhomogeneities in phantom. Quantitative mapping obtained with pRAFF showed minimal fluctuations across field inhomogeneities in vivo. Thus, pRAFF may be a promising tool for clinical applications where larger off-resonance resilience is needed at 3T, and further investigation of its sensitivity towards pathological remodeling is warranted.

4.6. Supporting Information

The following supporting information, describes the formulations of the effective field and locking field with their corresponding angle, respectively the tile angle and locking angle in the first and second RFR. Furthermore, the changing behavior of the simulated magnetization trajectory for all degrees of freedom and the line of optimal performance is shown in figure 4.6-4.9. Finally, the combined field inhomogeneity study in the calf is shown in figure 4.10.

During the presence of the (p)RAFF RF pulse, the field components can be described with their own formulation. $B_{eff}(t)$ is described with [26]:

$$B_{eff}(t) = \sqrt{B_1^2(t) + (\Delta\omega_1(t)/\gamma)^2} = \gamma^{-1} \sqrt{\omega_1^2(t) + \Delta\omega_1^2(t)}. \quad (4.9)$$

Here $B_1(t)$ is the time-dependent RF pulse amplitude, and the offset frequency ($\Delta\omega_1(t)$) relative to the Larmor frequency is given by:

$$\Delta\omega_1(t) = \omega_1(t) - \omega_0, \quad (4.10)$$

where $\omega_0 = \gamma B_0$ is the Larmor frequency, with γ the gyromagnetic ratio and B_0 the main magnetic field. From the offset frequency, the accumulated phase ($\varphi(t)$) can be obtained by:

$$\varphi(t) = \int_0^t \Delta\omega_1(\tau) d\tau. \quad (4.11)$$

The field strength of the effective field in the second RFR, $E(t)$, is composed of two components: the

effective field of the first RFR and the fictitious field $\left(\gamma^{-1} \frac{d\alpha(t)}{dt}\right)$ [8]:

$$E(t) = \sqrt{B_{eff}^2(t) + \left(\gamma^{-1} \frac{d\alpha(t)}{dt}\right)^2}, \quad (4.12)$$

with $\alpha(t)$ being the tilt angle, the angle between the \mathbf{z}' and $\mathbf{B}_{eff}(t)$ (Equation (4.13)) [8].

$$\alpha(t) = \arctan\left(\frac{\omega_1(t)}{\Delta\omega_1(t)}\right). \quad (4.13)$$

Generally, this angle $\varepsilon(t)$, the angle between $\mathbf{B}_{eff}(t)$ and $\mathbf{E}(t)$, can be calculated with [8]:

$$\varepsilon(t) = \arctan\left(\frac{\gamma^{-1} \frac{d\alpha(t)}{dt}}{B_{eff}(t)}\right). \quad (4.14)$$

Furthermore, the captions of the supplementary figures [figure 4.6-4.9](#):

SUPP. FIGURE 4.6 A) Radiofrequency shapes: amplitude modulation, frequency modulation, and phase for the changing parametric behavior of θ with respect to RAFF ($\theta = 0$ rad, $\nu = 1$ and $\rho = 1$) as default. B) Corresponding magnetization behavior for all RF shapes in the first rotating frame. Indicating the magnetization vector ($M(t)$, orange) with its trajectory and the effective field ($B_{eff}(t)$, blue).

SUPP. FIGURE 4.7 A) Radiofrequency shapes: amplitude modulation, frequency modulation, and phase for the changing parametric behavior of ρ with respect to RAFF ($\theta = 0$ rad, $\nu = 1$ and $\rho = 1$) as default. B) Corresponding magnetization behavior for all RF shapes in the first rotating frame. Indicating the magnetization vector ($M(t)$, orange) with its trajectory and the effective field ($B_{eff}(t)$, blue).

SUPP. FIGURE 4.8 A) Radiofrequency shapes: amplitude modulation, frequency modulation, and phase for the changing parametric behavior of ν with respect to RAFF ($\theta = 0$ rad, $\nu = 1$ and $\rho = 1$) as default. B) Corresponding magnetization behavior for all RF shapes in the first rotating frame. Indicating the magnetization vector ($M(t)$, orange) with its trajectory and the effective field ($B_{eff}(t)$, blue).

SUPP. FIGURE 4.9 A) Radiofrequency shapes: amplitude modulation, frequency modulation, and phase for the changing parametric behavior of the line $\rho = \nu\sqrt{2}$ with respect to RAFF ($\theta = 0$ rad, $\nu = 1$ and $\rho = 1$) as default. B) Corresponding magnetization behavior for all RF shapes in the first rotating frame. Indicating the magnetization vector ($M(t)$, orange) with its trajectory and the effective field ($B_{eff}(t)$, blue).

SUPP. FIGURE 4.10 In vivo maps, for both RAFF and pRAFF, for B_0 and B_1^+ inhomogeneities obtained for $\Delta\omega_1^{off} = [-150, 0, 150]$ Hz for each $\eta_1 = [0.5, 0.75, 1.0]$. Improved consistency is shown for pRAFF in the calf, with a coefficient of variation (CoV) of 6.5% as opposed to 78.3% for RAFF. All subfigures are respectively for RAFF and pRAFF. (A, B) The averaged relaxation times in the selected region of interest (ROI) of the calf muscle with (C, D) the corresponding maps for various field inhomogeneities.

4.7. Figures

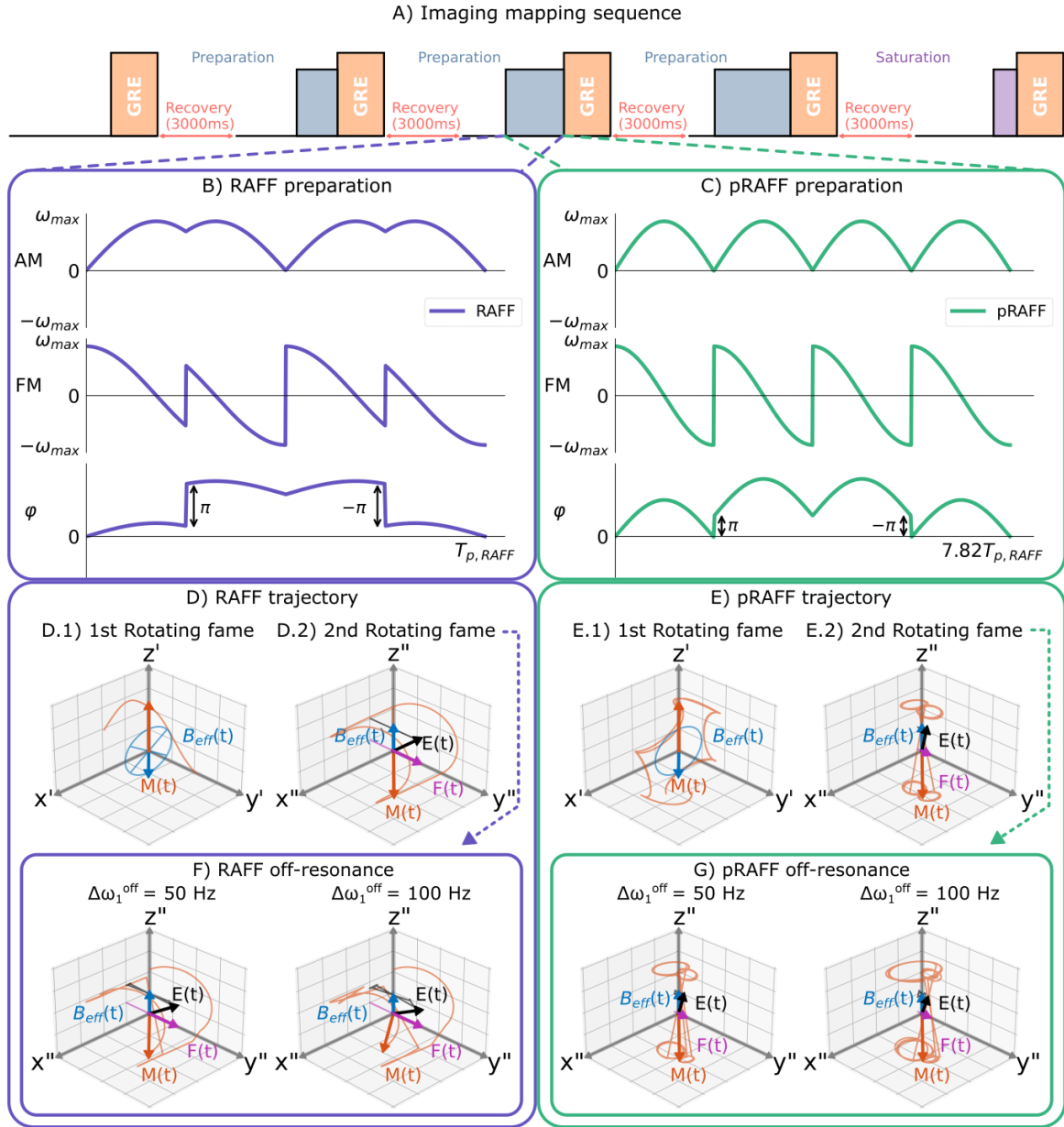


Figure 4.1: A) Schematic representation of the T_{RAFF} mapping sequence for 4 T_{RAFF} -prepared images (0, 28, 57, 85 ms) and one saturation image with a 3 s recovery in between acquisitions. (B, C) Radiofrequency shapes: amplitude modulation, frequency modulation, and phase for both RAFF ($\theta = 0$ rad, $\nu = 1$ and $\rho = 1$) and pRAFF ($\theta = 0$ rad, $\nu = 5.53$ and $\rho = 7.82$), respectively. (D, E) The corresponding magnetization behavior of RAFF and pRAFF pulses in two rotating frames. 1) The first rotating frame, denoted with x', y' and z' and oscillating at $\omega_1(t)$. 2) The second rotating frame, denoted with x'', y'' and z'' , where the z'' is aligned with the effective field. Indicating the magnetization vector ($M(t)$, orange) with its trajectory, the effective field ($B_{eff}(t)$, blue), the fictitious field ($F(t)$, pink), and the resulting field ($E(t)$, black). (F, G) The magnetization behavior at several off-resonances of RAFF and pRAFF in the second rotating frame. Increased off-resonance resilience for pRAFF is indicated with the better alignment of M with the z'' -axis for larger off-resonances.

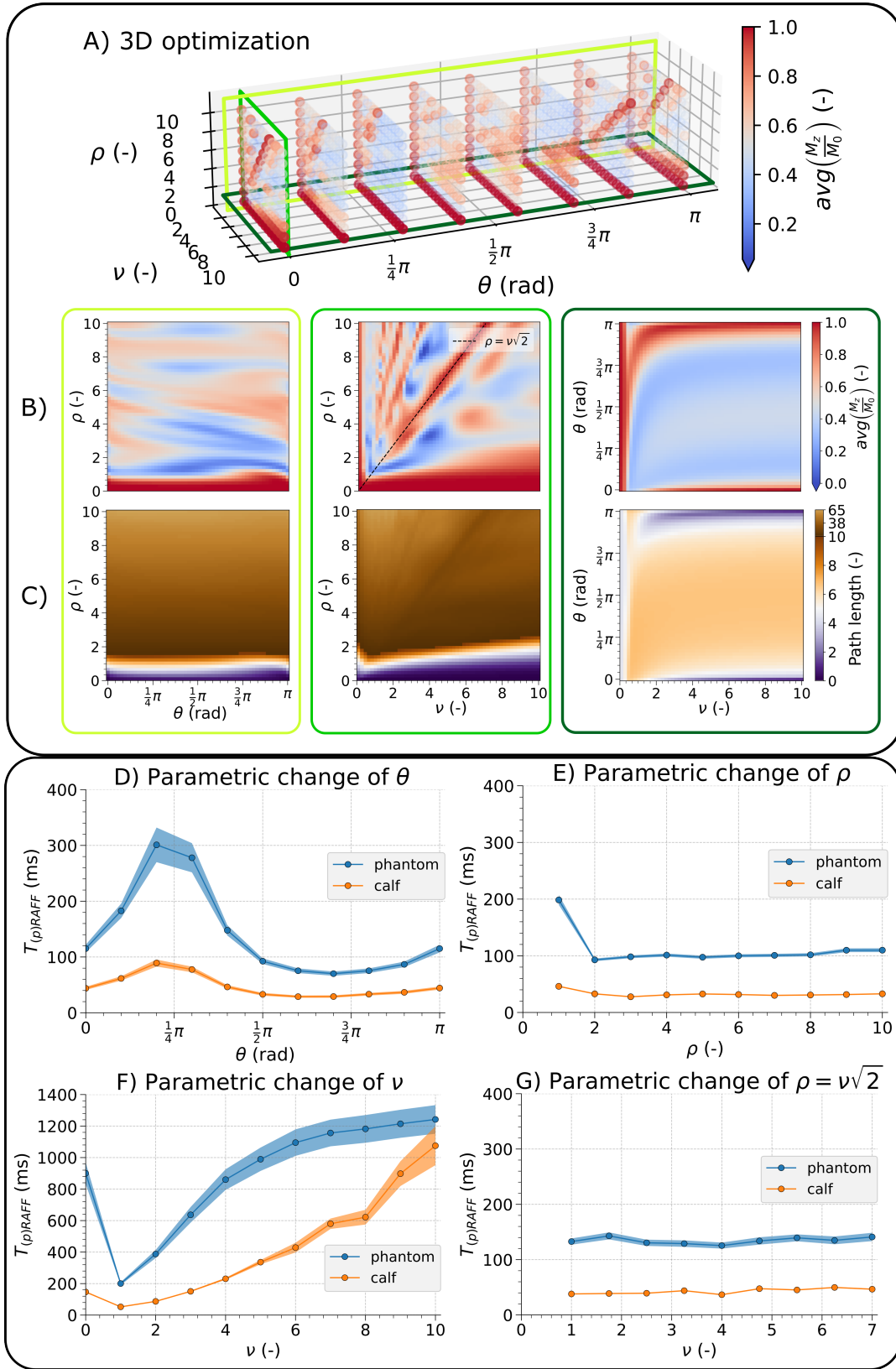


Figure 4.2: A) Visualization of the pulse efficiency for the pRAFF parameter space within the bounds: $(\theta, \nu, \rho) \in [0, \pi] \text{ rad} \times [0.1, 10] \times [0.1, 10]$. The pulse peak power was fixed to 500 Hz. For each parameter set the M_z/M_0 was averaged over the region $(\eta_1, \Delta\omega_1^{off}) \in [0.5, 1] \times [-400, 400] \text{ Hz}$ as a performance measure. The optimal shape parameters were determined as $\theta = 0 \text{ rad}$, $\nu = 5.53$ and $T_p = 7.82 T_{p,RAFF}$. (B, C) 2D parameter for each degree of freedom (DoF), fixing the third parameter to the original RAFF pulse ($\theta = 0 \text{ rad}$, $\nu = 1$ and $\rho = 1$), B) magnetization and C) path length, as a measure of spin-lock effectiveness, is presented. All 2D planes indicated an increased averaged M_z for small time durations and small values of ν , which was accompanied by a dramatic drop in path length. (D-G) Quantitative assessment of T_{pRAFF} for various parameter values in the TIMES [32] phantom and in the calf muscle to study the effect of parameter changes. Starting from the original RAFF pulse ($\theta = 0 \text{ rad}$, $\nu = 1$ and $\rho = 1$), T_{pRAFF} times were obtained by varying each parameter while keeping others parameters fixed at the original RAFF case. The parameters were varied along the following lines: D) $\theta = [0, 0.1\pi, \dots, \pi] \text{ rad}$, E) $\rho = [1, 2, 3, \dots, 10]$ and F) $\nu = [0.1, 1, 2, 3, \dots, 10]$. H) To include to optimal pulse, two parameters were varied along the line $\rho = \nu\sqrt{2}$ with $\nu = [1, 1.75, 2.5, \dots, 7]$. Phantom and calf results show good agreement for all parameter changes.

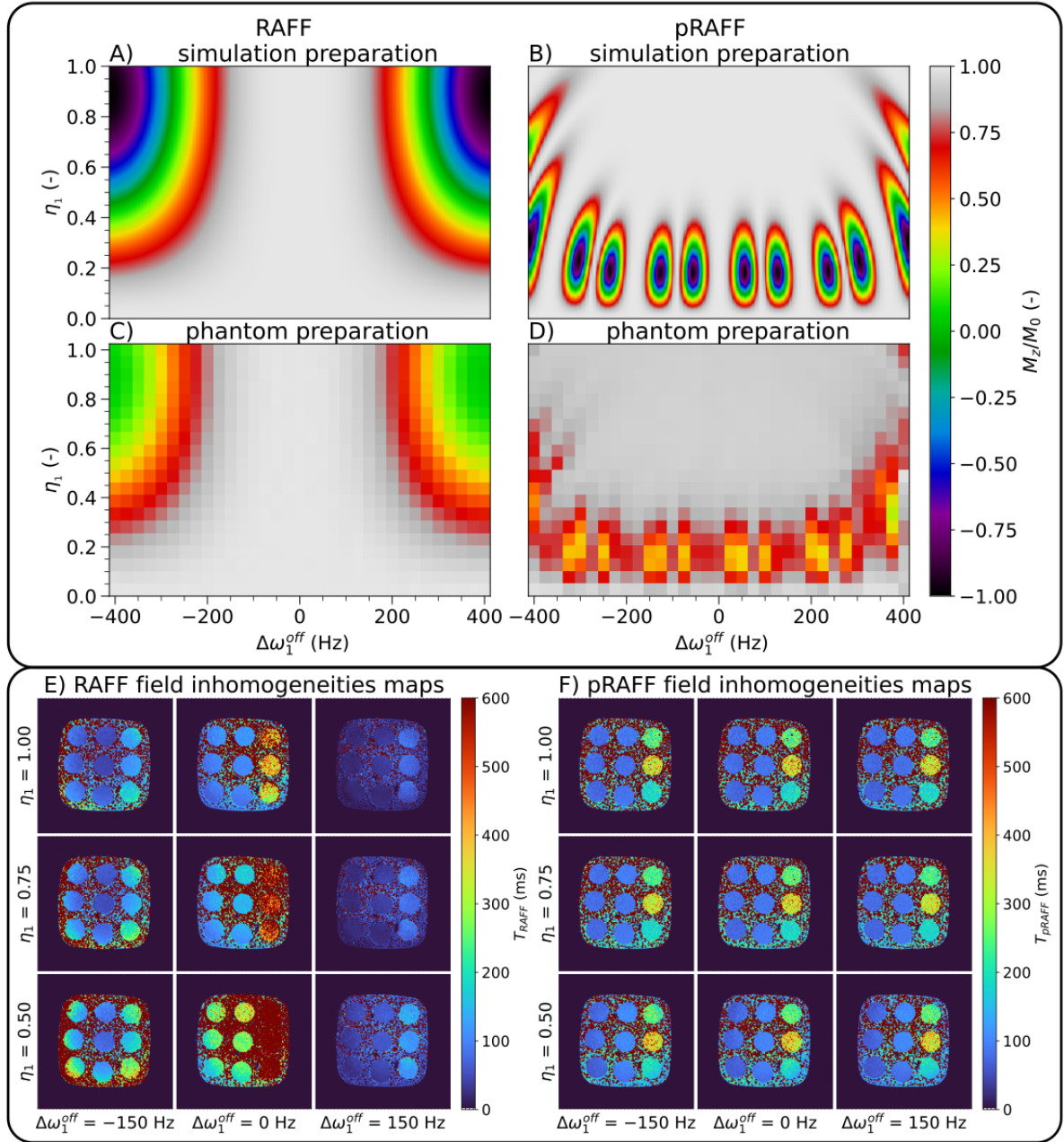


Figure 4.3: Improved resilience against field inhomogeneities is obtained for pRAFF compared to RAFF, shown in the enlarged off-resonance bandwidth for the homogeneous performance plane close to 1 (gray). For all field inhomogeneities, more consistent maps are obtained for pRAFF and RAFF, with a coefficient of variation (CoV) of 11% and 78.2%, respectively. (A-D) Preparation performance for relative B_0 and B_1^+ artifacts of M_z/M_0 obtained in (A, B) simulations and in (C, D) phantom. For a 500 Hz peak frequency, (A, C) preparation performance obtained with RAFF and (B, D) pRAFF pulse for $(\eta_1, \Delta\omega_1^{off}) \in [0, 1] \times [-400, 400]$ Hz. Here η_1 is the ratio between the effective and nominal B_1^+ power. In simulations, an average of 0.95 and 0.36 was measured for RAFF, and pRAFF, respectively. In the phantom, a single RAFF preparation of 2.8 ms resulted in an averaged M_z of 0.67 and a single pRAFF preparation ($7.82 T_{p,RAFF}$) resulted in an average of 0.91 for the upper half-plane. (E, F) Phantom maps, for both RAFF and pRAFF, for B_0 and B_1^+ inhomogeneities obtained for $\Delta\omega_1^{off} = [-150, 0, 150]$ Hz for each $\eta_1 = [0.5, 0.75, 1.0]$. For the RAFF pulse, signal drops and gains are visualized in several positions in the phantom maps.

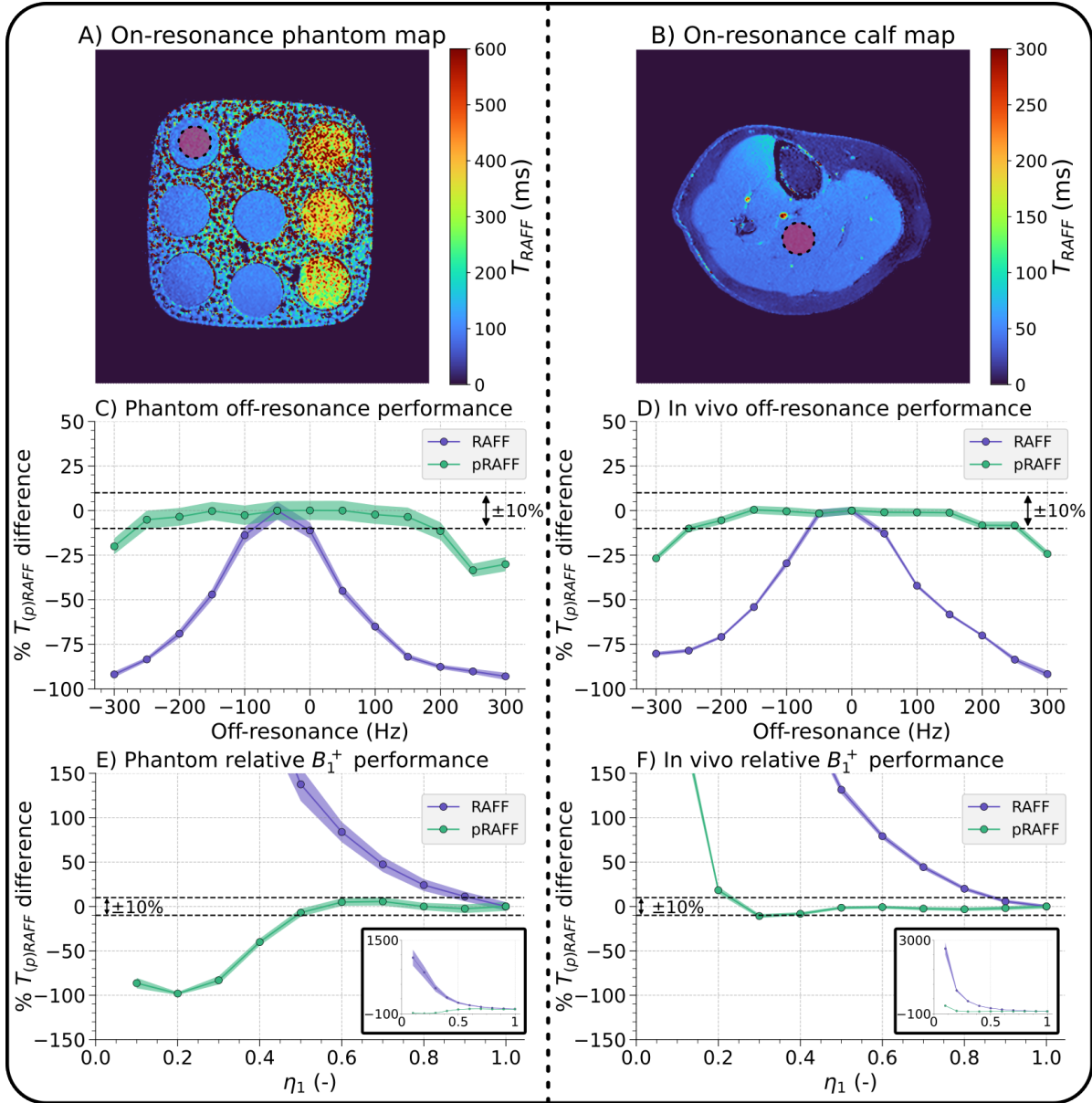


Figure 4.4: (A, B) Phantom and in vivo calf maps, respectively. For RAFF and pRAFF a circular region of interest (ROI) containing a vial or muscle tissue was selected to assess relaxation time for off-resonance and relative B_1^+ performance. (C, D) Off-resonance performance of RAFF and pRAFF (C) in the phantom and (D) in the calf muscle at 13 off-resonance frequencies $\Delta\omega_1^{off} = [-300, -250, \dots, 300]$ Hz with a peak frequency of 500 Hz ($B_{1,max}^+ = 11.74 \mu\text{T}$). (E, F) Relative B_1^+ performance of RAFF and pRAFF (E) in the phantom and (F) the calf muscle for 10 field inhomogeneities $\eta_1 = [0.1, 0.2, \dots, 1]$ without frequency offset. A complete overview of acquired data points is shown in the subfigure for relative B_1^+ performance. Increased off-resonance and relative B_1^+ performance is obtained for pRAFF compared to RAFF in the phantom and calf. In the range of $\pm 10\%$, T_{pRAFF} remains consistent for a 450 ± 30 Hz wide frequency range for pRAFF compared with 100 ± 20 Hz for RAFF in the phantom. In vivo, a 500 ± 15 Hz wide frequency range is obtained for pRAFF compared with 100 ± 10 Hz for RAFF. For relative B_1^+ performance, T_{pRAFF} the ranges are: $0.5 \leq \eta_1 \leq 1$ and $0.4 \leq \eta_1 \leq 1$ in the phantom and calf, respectively. T_{RAFF} exceeds the tolerance for $\eta_1 < 0.9$.

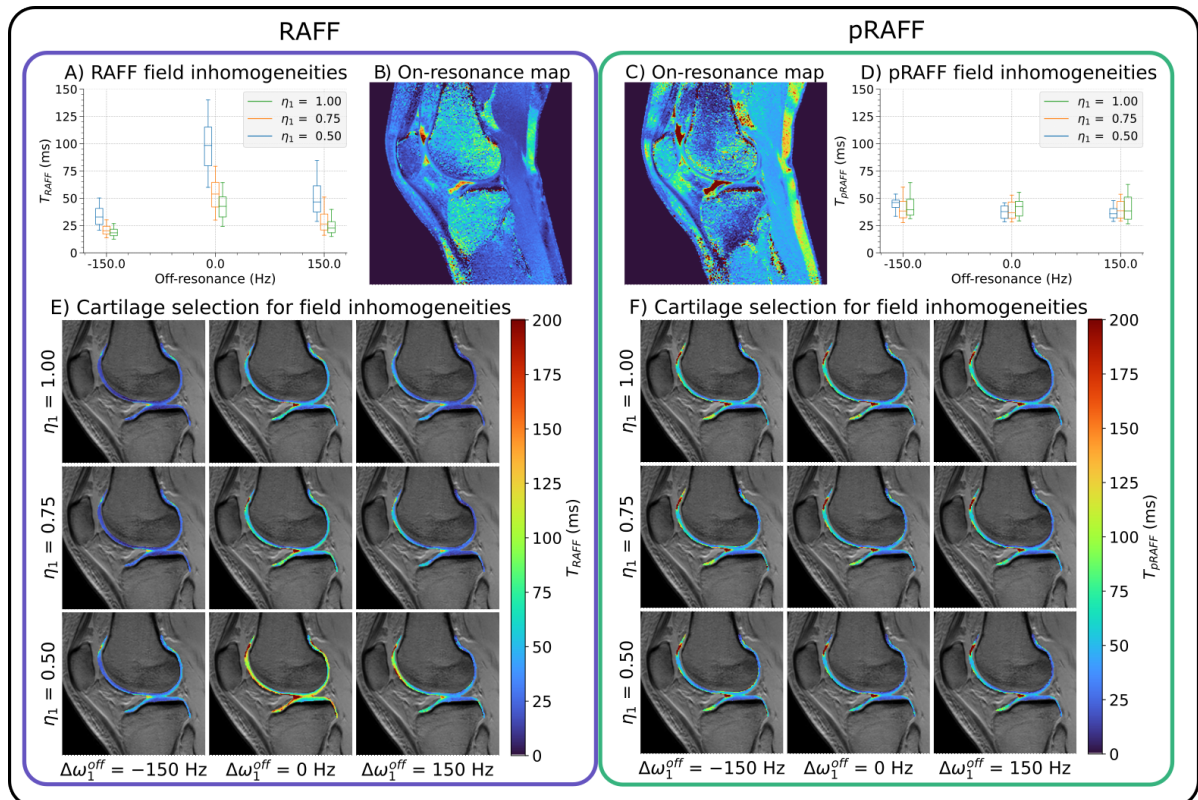
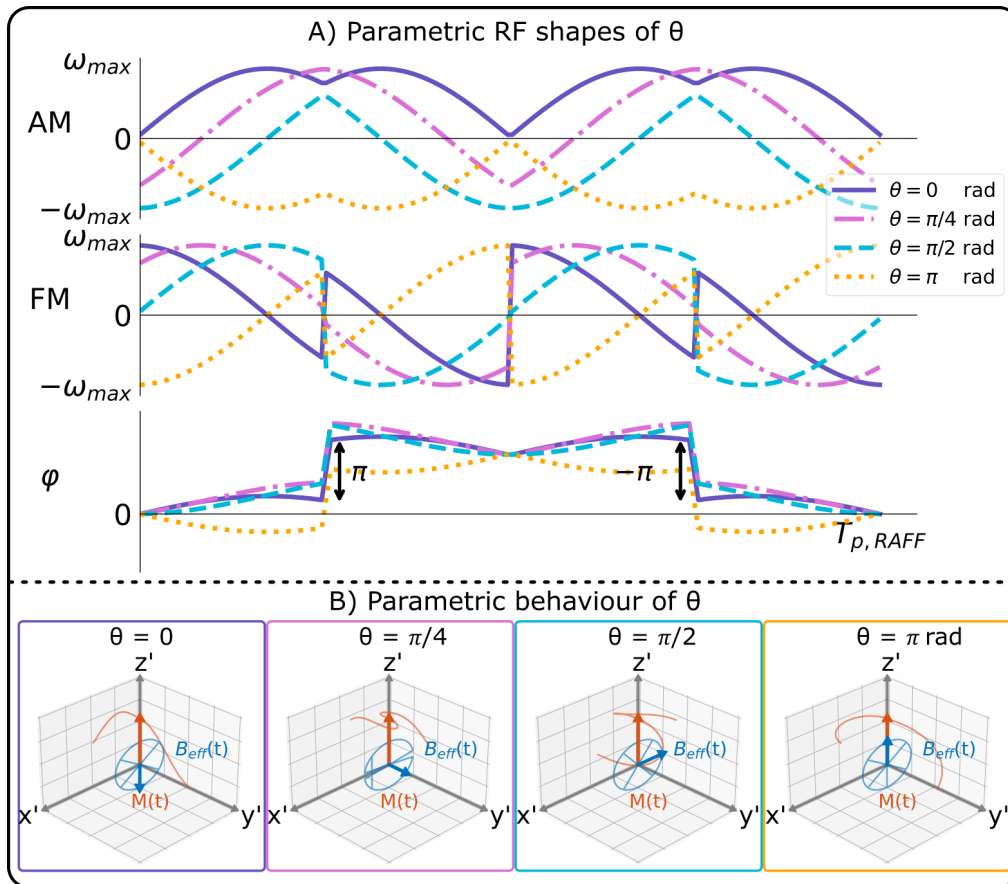
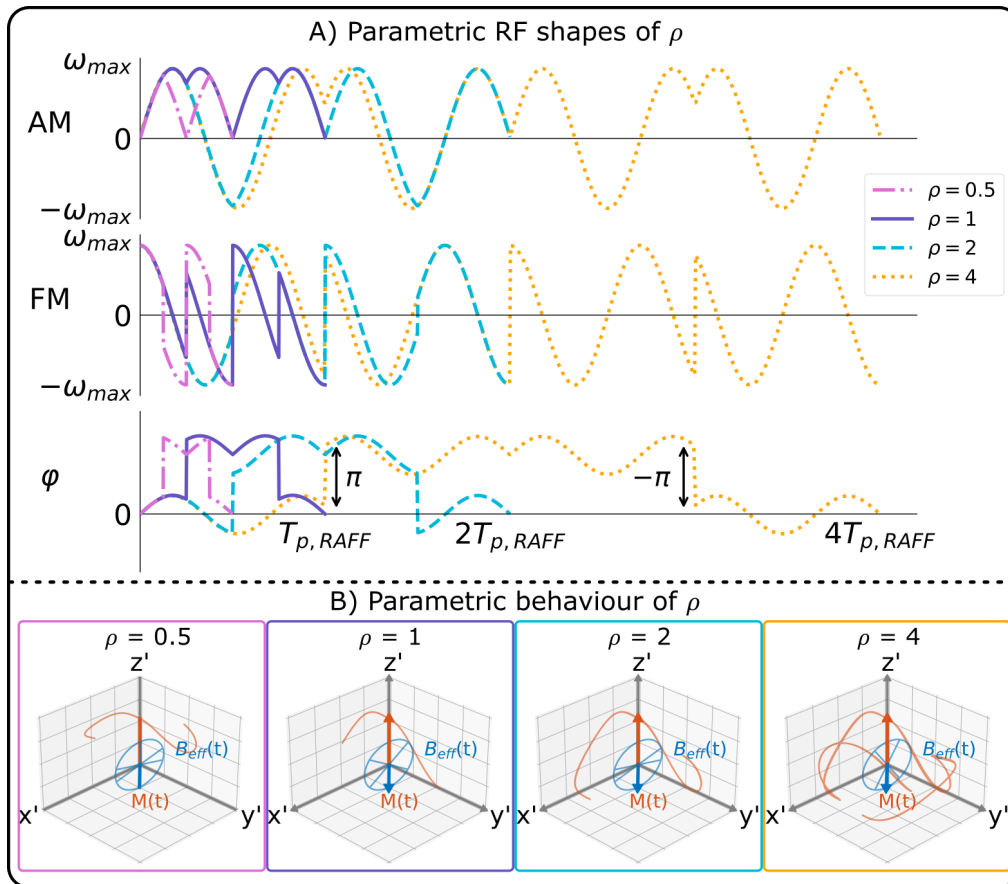


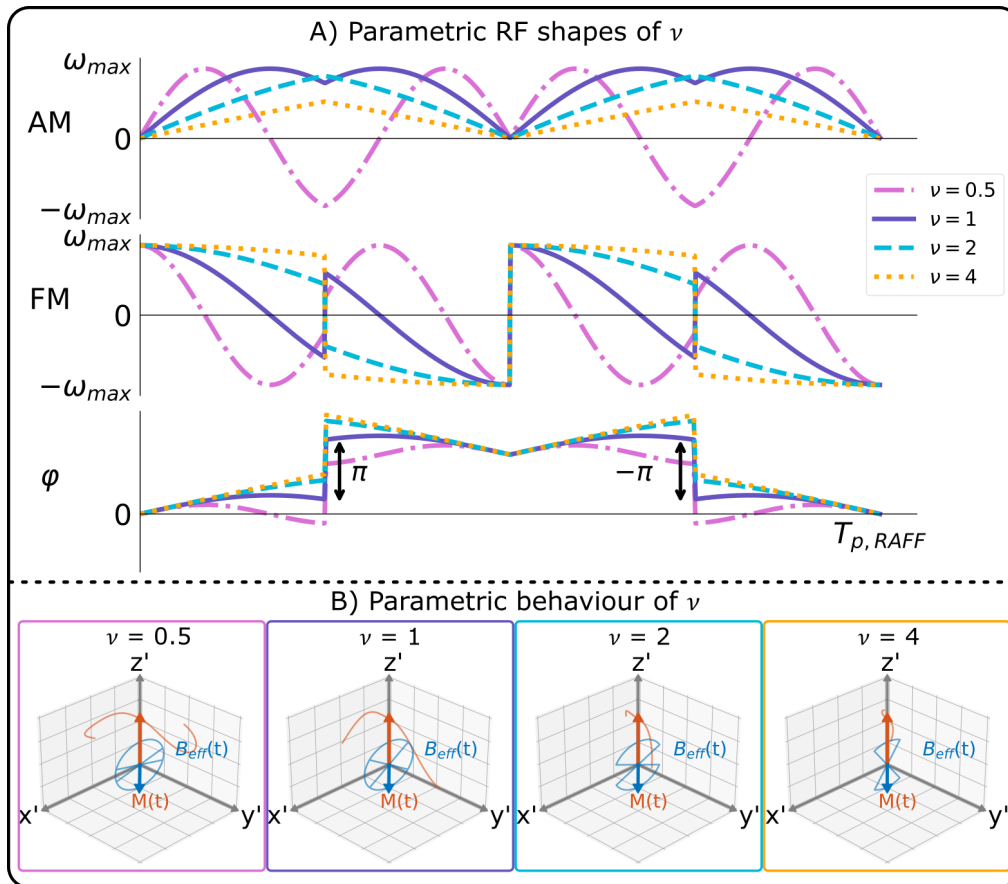
Figure 4.5: In vivo maps, for both RAFF and pRAFF, for B_0 and B_1^+ inhomogeneities obtained for $\Delta\omega_1^{off} = [-150, 0, 150]$ Hz for each $\eta_1 = [0.5, 0.75, 1.0]$. Improved consistency is shown for pRAFF in the knee cartilage, with a coefficient of variation (CoV) of 11% opposed to 57% for RAFF. All subfigures are respectively presented for RAFF and pRAFF (A, B) The averaged relaxation times of the knee cartilage region of interest (ROI). (C, D) In vivo T_{RAFF} and T_{pRAFF} knee maps acquired on-resonance, with the corresponding colormap in subfigures E and F. (E, F) Overlay of the RAFF and pRAFF-based maps in the cartilage with baseline images of the knee. Good consistency of the mapping results is obtained across all field inhomogeneities with pRAFF, while substantial fluctuation can be seen for RAFF.



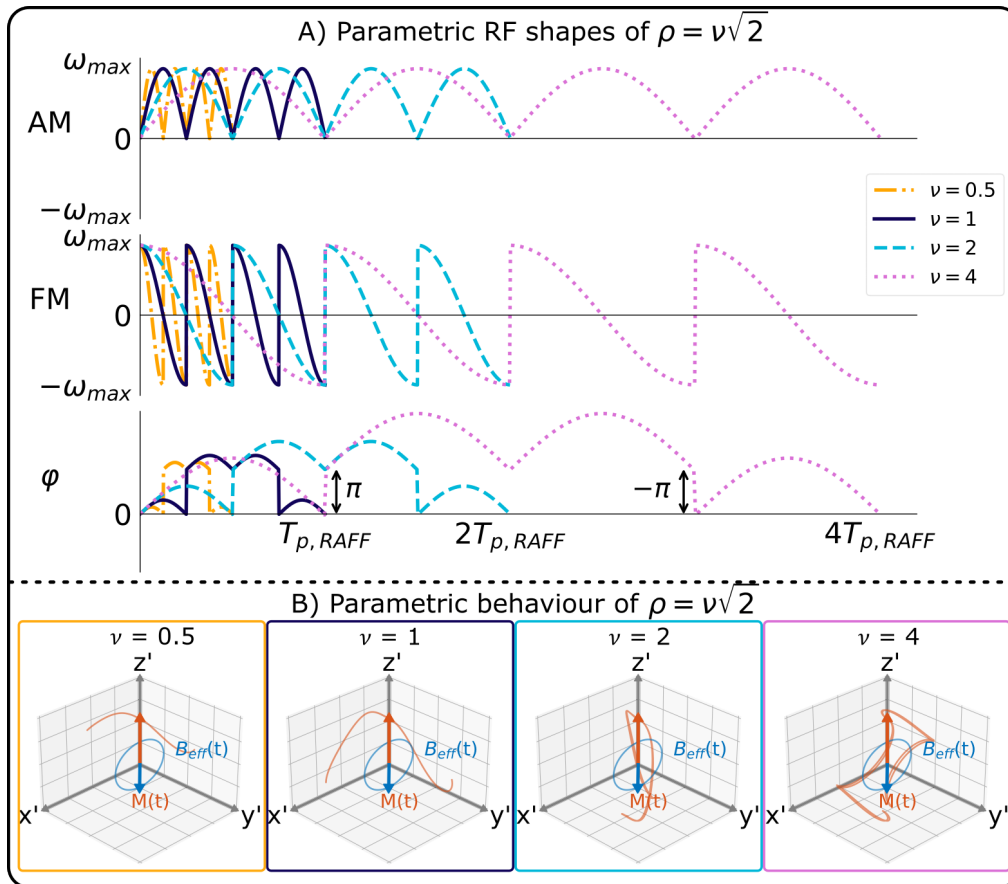
Supp. Figure 4.6: A) Radiofrequency shapes: amplitude modulation, frequency modulation, and phase for the changing parametric behavior of θ with respect to RAFF ($\theta = 0$ rad, $\nu = 1$ and $\rho = 1$) as default. B) Corresponding magnetization behavior for all RF shapes in the first rotating frame. Indicating the magnetization vector ($M(t)$, orange) with its trajectory and the effective field ($B_{eff}(t)$, blue).



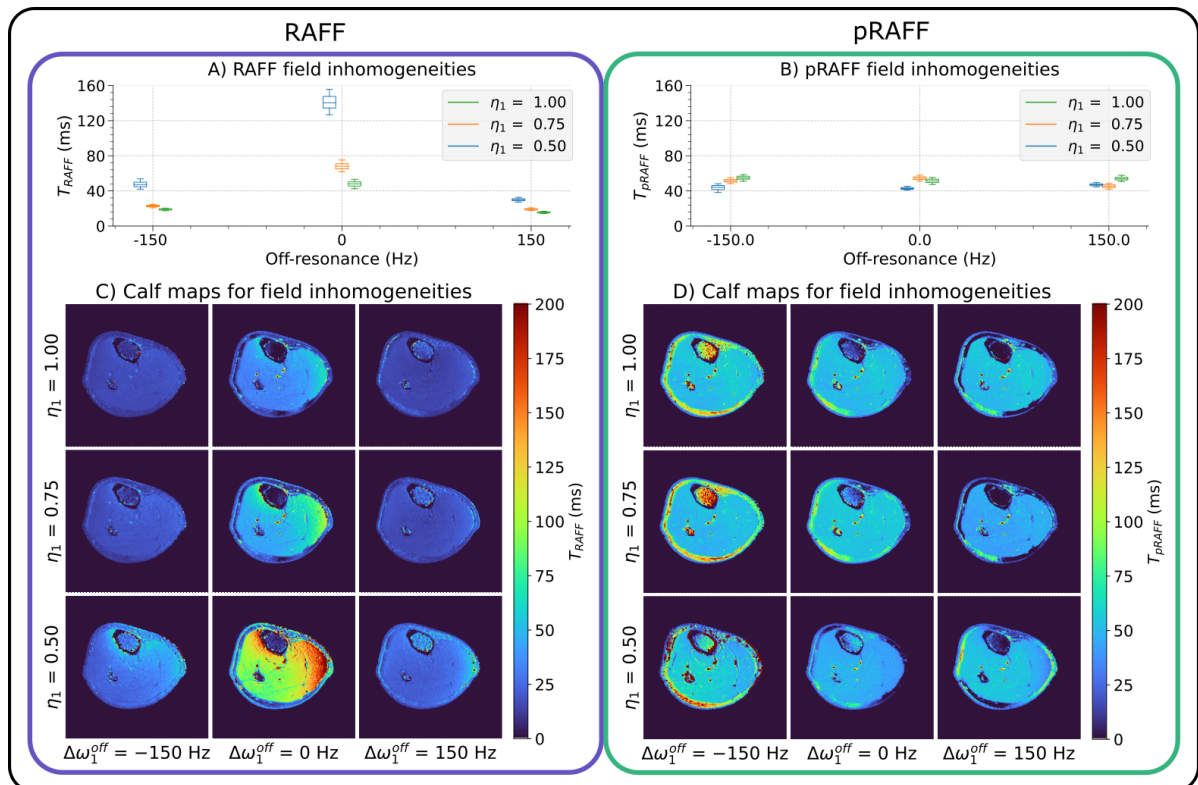
Supp. Figure 4.7: A) Radiofrequency shapes: amplitude modulation, frequency modulation, and phase for the changing parametric behaviour of ρ with respect to RAFF ($\theta = 0$ rad, $\nu = 1$ and $\rho = 1$) as default. B) Corresponding magnetization behaviour for all RF shapes in the first rotating frame. Indicating the magnetization vector ($M(t)$, orange) with its trajectory and the effective field ($B_{eff}(t)$, blue).



Supp. Figure 4.8: A) Radiofrequency shapes: amplitude modulation, frequency modulation, and phase for the changing parametric behaviour of ν with respect to RAFF ($\theta = 0$ rad, $\nu = 1$ and $\rho = 1$) as default. B) Corresponding magnetization behaviour for all RF shapes in the first rotating frame. Indicating the magnetization vector ($M(t)$, orange) with its trajectory and the effective field ($B_{eff}(t)$, blue).



Supp. Figure 4.9: A) Radiofrequency shapes: amplitude modulation, frequency modulation, and phase for the changing parametric behaviour of the line $\rho = \nu\sqrt{2}$ with respect to RAFF ($\theta = 0$ rad, $\nu = 1$ and $\rho = 1$) as default. B) Corresponding magnetization behaviour for all RF shapes in the first rotating frame. Indicating the magnetization vector ($M(t)$, orange) with its trajectory and the effective field ($B_{eff}(t)$, blue).



Supp. Figure 4.10: In vivo maps, for both RAFF and pRAFF, for B_0 and B_1^+ inhomogeneities obtained for $\Delta\omega_1^{off} = [-150, 0, 150]$ Hz for each $\eta_1 = [0.5, 0.75, 1.0]$. Improved consistency is shown for pRAFF in the calf, with a coefficient of variation (CoV) of 6.5% as opposed to 78.3% for RAFF. All subfigures are respectively for RAFF and pRAFF. (A, B) The averaged relaxation times in the selected region of interest (ROI) of the calf muscle with (C, D) the corresponding maps for various field inhomogeneities.

5

Outlook

The objective of this project is to develop new contrasts for quantitative MRI (qMRI) through research into the performance of recently developed radiofrequency (RF) pulses. The overall aim is to minimize the susceptibility to off-resonance and B_1^+ artifacts in these pulses, using Relaxation along Fictitious Field (RAFF) as a starting point for their design. Throughout the project numerical simulations, phantom and in vivo measurements were conducted to study the newly proposed RF pulses. Finally, parametric RAFF (pRAFF) pulses were proposed and optimized for 3 degrees of freedom with Bloch simulations. The best preparation efficiency was achieved by identifying the optimal combination of parameters. The parametric study of pRAFF has revealed that a decrease in path length leads to a loss of contrast-to-noise ratio (CNR). Hence, to ensure sufficient CNR, it was essential to maintain a minimum path length, which serves as an indicator of spin-lock efficiency.

RAFF has demonstrated limited resilience to field inhomogeneities in both phantom and calf experiments. However, by expanding the parametric space and decoupling the effective field strength from the fictitious field strength in pRAFF, the field inhomogeneity resilience was further improved, resulting in a 5 times higher resilience to off-resonance and B_1^+ inhomogeneities in both phantom and calf experiments. At 3T, pRAFF was able to maintain consistency for in vivo relaxation time mappings across multiple field inhomogeneities in the cartilage, with a coefficient of variation of 11% compared to 57% for RAFF. At the same time for reproducibility, minimal fluctuations were shown across several healthy subjects. Therefore, T_{pRAFF} mapping has the potential to be a valuable clinical tool in situations where greater off-resonance resilience is required.

Further work can be done to study other pulses. This work was focused on optimizing RAFF pulses, but as derived in the appendix several other pulses exist. Since they arose from specifying different conditions for the excitation pulse. Condition as a locked effective field, or a constant fictitious field, constant effective field in the second rotating frame of reference, equally effective and fictitious field strength, or a locked effective field in the second rotating frame of reference. These RF pulses may have interesting characteristics as well. For sure, they will not give the optimal performance directly out of the box. Optimization can be done in a similar fashion as this report has shown. Extending the parametric space and optimization pulses in simulation to find an optimum within a bounded region and with bounding criteria.

The optimal performance and improved resilience against field inhomogeneities were found to move from the sub-adiabatic to the adiabatic regime. Extending this trend, it can be interesting to look at RAFF as a locking field in the first rotating frame and study its characteristics. Moreover, even though the RAFF field inhomogeneity resilience is increased for pRAFF, its sensitivity to tissue types has been changed. In a similar fashion, its function as biomarker for certain diseases is possibly adapted. Thus, clinical studies are an interesting topic for further research, for instance in patients with osteoarthritis or myocardial disease. Conducting scans on multiple subjects and scanners would as well aid to evaluate consistency across diverse situations.

Bibliography

- [1] Allen D Elster. *Making an Image - Questions and Answers in MRI*. 2021. URL: <https://www.mriquestions.com/hellipmaking-an-image.html>.
- [2] Center for Devices and Radiological Health. *Benefits and risks*. 2017. URL: <https://www.fda.gov/radiation-emitting-products/mri-magnetic-resonance-imaging/benefits-and-risks>.
- [3] Matt T. Cashmore et al. *Clinical quantitative MRI and the need for metrology*. 2021. DOI: [10.1259/bjr.20201215](https://doi.org/10.1259/bjr.20201215).
- [4] Kathryn E. Keenan et al. *Quantitative magnetic resonance imaging phantoms: A review and the need for a system phantom*. 2018. DOI: [10.1002/mrm.26982](https://doi.org/10.1002/mrm.26982).
- [5] Nikolaus Weiskopf et al. "Quantitative multi-parameter mapping of R1, PD*, MT, and R2* at 3T: A multi-center validation". In: *Frontiers in Neuroscience* 7 JUN (2013). ISSN: 1662453X. DOI: [10.3389/fnins.2013.00095](https://doi.org/10.3389/fnins.2013.00095).
- [6] Abdul Wahed Kajabi et al. "Evaluation of articular cartilage with quantitative MRI in an equine model of post-traumatic osteoarthritis". In: *Journal of Orthopaedic Research* 39.1 (2021). ISSN: 1554527X. DOI: [10.1002/jor.24780](https://doi.org/10.1002/jor.24780).
- [7] Seyed Amir Mirmojarabian et al. "Myocardium Assessment by Relaxation along Fictitious Field, Extracellular Volume, Feature Tracking, and Myocardial Strain in Hypertensive Patients with Left Ventricular Hypertrophy". In: *International Journal of Biomedical Imaging* 2022 (2022). ISSN: 1687-4188.
- [8] Timo Liimatainen et al. "MRI contrast from relaxation along a fictitious field (RAFF)". In: *Magnetic Resonance in Medicine* 64.4 (2010), pp. 983–994. ISSN: 15222594. DOI: [10.1002/MRM.22372](https://doi.org/10.1002/MRM.22372).
- [9] Ligong Wang et al. "T1rho MRI of Menisci and Cartilage in Patients with Osteoarthritis at 3T". In: *European journal of radiology* 81.9 (Sept. 2012), p. 2329. ISSN: 0720048X. DOI: [10.1016/J.EJRAD.2011.07.017](https://doi.org/10.1016/J.EJRAD.2011.07.017). URL: [/pmc/articles/PMC3298732/%20/pmc/articles/PMC3298732/?report=abstract%20https://www.ncbi.nlm.nih.gov/pmc/articles/PMC3298732/](https://pubmed.ncbi.nlm.nih.gov/20https://www.ncbi.nlm.nih.gov/pmc/articles/PMC3298732/).
- [10] Mohammad Haris et al. "T1rho MRI and CSF biomarkers in diagnosis of Alzheimer's disease". In: *NeuroImage: Clinical* 7 (2015). ISSN: 22131582. DOI: [10.1016/j.nicl.2015.02.016](https://doi.org/10.1016/j.nicl.2015.02.016).
- [11] Timo Liimatainen et al. "MRI contrasts in high rank rotating frames". In: *Magnetic Resonance in Medicine* 73.1 (2015). ISSN: 15222594. DOI: [10.1002/mrm.25129](https://doi.org/10.1002/mrm.25129).
- [12] Driss Cammoun, Kathleen A Davis, and William R Hendee. "Clinical applications of magnetic resonance imaging—Current status". In: *Western Journal of Medicine* 143.6 (1985), p. 793.
- [13] Mehmet Akcakaya, Mariya Doneva, and Claudia Prieto. *Magnetic Resonance Image Reconstruction Theory, Methods, and Applications*. Academic Press 2022, 2022, p. 516. ISBN: 9780128227268.
- [14] Allen D Elster. "Questions and Answers in MRI". In: *Elster AD LLC* (2021).
- [15] Bernd André Jung and Matthias Weigel. *Spin echo magnetic resonance imaging*. 2013. DOI: [10.1002/jmri.24068](https://doi.org/10.1002/jmri.24068).
- [16] David Felson et al. "Progression of osteoarthritis as a state of inertia". In: *Annals of the Rheumatic Diseases* 72.6 (2013). ISSN: 00034967. DOI: [10.1136/annrheumdis-2012-201575](https://doi.org/10.1136/annrheumdis-2012-201575).
- [17] T. Neogi. "The epidemiology and impact of pain in osteoarthritis". In: *Osteoarthritis and Cartilage* 21.9 (2013). ISSN: 10634584. DOI: [10.1016/j.joca.2013.03.018](https://doi.org/10.1016/j.joca.2013.03.018).
- [18] J. A. Buckwalter and H. J. Mankin. *Articular cartilage: degeneration and osteoarthritis, repair, regeneration, and transplantation*. 1998.
- [19] Jari Rautiainen et al. "Multiparametric MRI assessment of human articular cartilage degeneration: Correlation with quantitative histology and mechanical properties". In: *Magnetic Resonance in Medicine* 74.1 (2015). ISSN: 15222594. DOI: [10.1002/mrm.25401](https://doi.org/10.1002/mrm.25401).

- [20] Yuanyuan Wang et al. *Use magnetic resonance imaging to assess articular cartilage*. 2012. DOI: [10.1177/1759720X11431005](https://doi.org/10.1177/1759720X11431005).
- [21] Mikko J. Nissi et al. "Multi-parametric MRI characterization of enzymatically degraded articular cartilage". In: *Journal of Orthopaedic Research* 34.7 (2016). ISSN: 1554527X. DOI: [10.1002/jor.23127](https://doi.org/10.1002/jor.23127).
- [22] Yang Xia. "Relaxation anisotropy in cartilage by NMR microscopy (muMRI) at 14-microm resolution". In: *Magnetic resonance in medicine* 39.6 (1998), pp. 941–949. ISSN: 0740-3194. DOI: [10.1002/MRM.1910390612](https://doi.org/10.1002/MRM.1910390612). URL: <https://pubmed.ncbi.nlm.nih.gov/9621918/>.
- [23] Jun Hirose et al. "T1 ρ and T2 mapping of the proximal tibiofibular joint in relation to aging and cartilage degeneration". In: *European Journal of Radiology* 81.10 (2012). ISSN: 0720048X. DOI: [10.1016/j.ejrad.2011.11.019](https://doi.org/10.1016/j.ejrad.2011.11.019).
- [24] Mathieu Boudreau, Kathryn E. Keenan, and Nikola Stikov. "Quantitative T1 and T1 ρ Mapping". In: 1 (Jan. 2020), pp. 19–45. ISSN: 2666-9099. DOI: [10.1016/B978-0-12-817057-1.00004-4](https://doi.org/10.1016/B978-0-12-817057-1.00004-4).
- [25] Yuchi Han et al. *Assessing Myocardial Disease Using T1 ρ MRI*. 2014. DOI: [10.1007/s12410-013-9248-7](https://doi.org/10.1007/s12410-013-9248-7).
- [26] Michael Garwood and Lance DelaBarre. "The Return of the Frequency Sweep: Designing Adiabatic Pulses for Contemporary NMR". In: *Journal of Magnetic Resonance* 153.2 (Dec. 2001), pp. 155–177. ISSN: 1090-7807. DOI: [10.1006/JMRE.2001.2340](https://doi.org/10.1006/JMRE.2001.2340).
- [27] A. F. Martino and R. Damadian. "Improved discrimination of normal and malignant tissue using 1H NMR relaxation time measurements at 2.18 MHz." In: *Physiological chemistry and physics and medical NMR* 16.1 (1984). ISSN: 07486642.
- [28] Joao Tourais et al. "2D High Resolution Myocardial TRAFF2 Mapping: Reproducibility and Accuracy". In: *Proc. Intl. Soc. Mag. Reson. Med.* Vol. 29. 2021, p. 993.
- [29] J. Rautiainen et al. "Adiabatic rotating frame relaxation of MRI reveals early cartilage degeneration in a rabbit model of anterior cruciate ligament transection". In: *Osteoarthritis and Cartilage* 22.10 (2014). ISSN: 15229653. DOI: [10.1016/j.joca.2014.04.023](https://doi.org/10.1016/j.joca.2014.04.023).
- [30] Guido Van Rossum et al. *Python 3 Reference Manual*. Vol. 585. 7825. 2009.
- [31] Mehmet Akçakaya et al. "Improved quantitative myocardial T2 mapping: Impact of the fitting model". In: *Magnetic Resonance in Medicine* 74.1 (2015). ISSN: 15222594. DOI: [10.1002/mrm.25377](https://doi.org/10.1002/mrm.25377).
- [32] Gabriella Captur et al. "A medical device-grade T1 and ECV phantom for global T1 mapping quality assurance - the T1 Mapping and ECV Standardization in cardiovascular magnetic resonance (T1MES) program". In: *Journal of Cardiovascular Magnetic Resonance* 18.1 (2016). ISSN: 1532429X. DOI: [10.1186/s12968-016-0280-z](https://doi.org/10.1186/s12968-016-0280-z).
- [33] Jutta Ellermann et al. "MRI rotating frame relaxation measurements for articular cartilage assessment". In: *Magnetic Resonance Imaging* 31.9 (2013). ISSN: 0730725X. DOI: [10.1016/j.mri.2013.06.004](https://doi.org/10.1016/j.mri.2013.06.004).

Appendices

A. Pulse Derivations

The spectrum for sub-adiabatic, adiabatic and locking fields started along the derivations discussed in this section. There several possible RF-pulse are derived, besides the case of constant effective, which is extensively studied in this report. There are the conditions of a locked effective field, or a constant fictitious field, constant effective field in the second rotating frame of reference, equally effective and fictitious field strength or a locked effective field in the second rotating frame of reference. RF pulses solutions for all cases are shown blown.

Already, for later reference the derivative of the arctan $\left(\frac{A(t)}{B(t)}\right)$:

$$\frac{d \arctan\left(\frac{A(t)}{B(t)}\right)}{dt} = \frac{\frac{dA(t)}{dt} B(t) - \frac{dB(t)}{dt} A(t)}{A^2(t) + B^2(t)}. \quad (1)$$

A.1. Problem: Constant Effective Field

For which amplitude and frequency-modulated RF-pulse shapes is the effective field constant and holds the following equation:

$$B_{eff}(t) = const. \quad (2)$$

Derivation

Start with the problem, a constant field means:

$$\frac{dB_{eff}(t)}{dt} = 0.$$

This can be explicitly written as:

$$\frac{dB_{eff}(t)}{dt} = \gamma^{-1} \frac{\frac{d\omega_1(t)}{dt} \omega_1(t) + \frac{d\Delta\omega_1(t)}{dt} \Delta\omega_1(t)}{\sqrt{\omega_1^2(t) + \Delta\omega_1^2(t)}} = 0.$$

At the same time this means:

$$\begin{cases} \frac{d\omega_1(t)}{dt} \omega_1(t) + \frac{d\Delta\omega_1(t)}{dt} \Delta\omega_1(t) = 0; \\ \omega_1^2(t) + \Delta\omega_1^2(t) \neq 0. \end{cases} \quad (3)$$

First Solution

Equation 3 has at least these four solutions, the first solution:

$$\begin{aligned} \frac{d\omega_1(t)}{dt} = 0 \wedge \frac{d\Delta\omega_1(t)}{dt} = 0; \\ \Rightarrow \omega_1(t) = c_1 \wedge \Delta\omega_1(t) = c_2, \end{aligned}$$

with c_1 and c_2 being constants. Hence, equation 4 is satisfied as long as both functions $(\omega_1(t))$ and $(\Delta\omega_1(t))$ are real and are not the 0 function.

Second Solution

The second solution of [equation 3](#):

$$\begin{aligned}\omega_1(t) &= -\Delta\omega_1(t) \wedge \frac{d\Delta\omega_1(t)}{dt} = \frac{d\omega_1(t)}{dt}; \\ \Rightarrow \omega_1(t) &= -\Delta\omega_1(t) \wedge \frac{d\Delta\omega_1(t)}{dt} = -\frac{d\Delta\omega_1(t)}{dt}; \\ \Rightarrow \omega_1(t) &= -\Delta\omega_1(t) \wedge \frac{d\Delta\omega_1(t)}{dt} = 0; \\ \Rightarrow \omega_1(t) &= c_1 \quad \wedge \Delta\omega_1(t) = -c_1,\end{aligned}$$

with c_1 and c_2 being constants. [equation 4](#) is again satisfied, as long as both functions ($\omega_1(t)$ and $\Delta\omega_1(t)$) are real and are not the 0 function.

Third Solution

The third solution of [equation 3](#):

$$\begin{aligned}\frac{d\omega_1(t)}{dt} &= \Delta\omega_1(t) \wedge \frac{d\Delta\omega_1(t)}{dt} = -\omega_1(t); \\ \Rightarrow \frac{d^2\Delta\omega_1(t)}{dt^2} &= -\Delta\omega_1(t) \wedge \frac{d\Delta\omega_1(t)}{dt} = -\omega_1(t); \\ \Rightarrow \omega_1(t) &= -ic_3e^{it} + ic_4e^{-it} \wedge \Delta\omega_1(t) = c_3e^{it} + c_4e^{-it}; \\ \Rightarrow \omega_1(t) &= c_1 \sin(t) - c_2 \cos(t) \wedge \Delta\omega_1(t) = c_1 \cos(t) + c_2 \sin(t),\end{aligned}$$

with i the imaginary unit, c_1, c_2, c_3 and c_4 being constants. [equation 4](#) is again satisfied as, as long as both c_1 and c_2 are not 0:

$$(-ic_3e^{it} + ic_4e^{-it})^2 + (c_3e^{it} + c_4e^{-it})^2 = 2c_3c_4 \neq 0 \quad \forall t.$$

Fourth Solution

The fourth solution of [equation 3](#) is:

$$\begin{aligned}\omega_1(t) &= \frac{c_1}{\cosh(t)} \wedge \Delta\omega_1(t) = c_1 \tanh(t); \\ \Rightarrow \frac{d\omega_1(t)}{dt} &= -c_1 \frac{\tanh(t)}{\cosh(t)} \wedge \frac{d\Delta\omega_1(t)}{dt} = \frac{c_1}{\cosh^2(t)},\end{aligned} \tag{5}$$

This satisfies:

$$\frac{d\omega_1(t)}{dt} \omega_1(t) = -c_1^2 \frac{\tanh(t)}{\cosh^2(t)} = -\frac{d\Delta\omega_1(t)}{dt} \Delta\omega_1(t).$$

[Equation 4](#) is again satisfied since:

$$\omega_1^2(t) + \Delta\omega_1^2(t) = c_1^2,$$

and this directly shows that [equation 2](#) holds.

Conclusion

For the problem, as defined in [equation 2](#), the pulse shapes for a constant effective field.

In the end, there are four possible solutions. There are two solutions when $\omega_1(t)$ and $\Delta\omega_1(t)$ are not the 0 function and real:

$$\begin{aligned}\omega_1(t) &= c_1, \quad c_1, \frac{c_1}{\cosh(t)}; \\ \Delta\omega_1(t) &= c_2, -c_1, c_1 \tanh(t),\end{aligned} \tag{6}$$

and there is one possible solution when both constants c_1 and c_2 are not 0:

$$\begin{aligned}\omega_1(t) &= c_1 \sin(t) - c_2 \cos(t); \\ \Delta\omega_1(t) &= c_1 \cos(t) + c_2 \sin(t).\end{aligned} \tag{7}$$

A.2. Problem: Locked Effective Field or Constant Fictitious Field

For which amplitude and frequency-modulated RF-pulse shapes is the angle of the effective field locked and holds the following equation: This equality can only be true when:

$$\frac{d\alpha(t)}{dt} = 0 \quad \forall t. \quad (8)$$

Derivation

Start with the problem and considering the derivative of the arctan in [equation 1](#), the following should be valid:

$$\frac{\frac{d\omega_1(t)}{dt} \Delta\omega_1(t) - \frac{d\Delta\omega_1(t)}{dt} \omega_1(t)}{\omega_1^2(t) + \Delta\omega_1^2(t)} = 0.$$

At the same time this results in:

$$\begin{cases} \frac{d\omega_1(t)}{dt} \Delta\omega_1(t) - \frac{d\Delta\omega_1(t)}{dt} \omega_1(t) = 0; \\ \omega_1^2(t) + \Delta\omega_1^2(t) \neq 0. \end{cases} \quad (9)$$

(10)

[Equation 9](#) has at least these two solutions.

First and General Solution

The first solution of [equation 9](#):

$$\begin{aligned} \frac{d\omega_1(t)}{dt} &= \frac{d\Delta\omega_1(t)}{dt} \wedge \omega_1(t) = \Delta\omega_1(t); \\ &\Rightarrow \omega_1(t) = c_1 \Delta\omega_1(t). \end{aligned}$$

Hence, [equation 10](#) is satisfied as long as both functions ($\omega_1(t)$ and $\Delta\omega_1(t)$) are real and are not the 0 function.

$$\omega_1^2(t) + \Delta\omega_1^2(t) = (c_1^2 + 1)\Delta\omega_1^2(t) \neq 0 \quad \forall t.$$

First Special Case

The second solution of [equation 9](#):

$$\begin{aligned} \frac{d\omega_1(t)}{dt} &= c_2 \omega_1(t) \wedge \frac{d\Delta\omega_1(t)}{dt} = c_2 \Delta\omega_1(t); \\ &\Rightarrow \omega_1(t) = c_1 e^{c_2 t} \wedge \Delta\omega_1(t) = e^{c_2 t}, \end{aligned}$$

with c_1 , c_2 and c_3 being constants. [Equation 10](#) is again satisfied as, as long as both $\omega_1(t)$ and $\Delta\omega_1(t)$ are not the 0 function:

$$(c_1 e^{c_2 t})^2 + (e^{c_2 t})^2 = c_1^2 e^{2c_2 t} + e^{2c_2 t} \neq 0 \quad \forall t.$$

Second Special Case

The third solution of [equation 9](#) is a special solution and based on a symmetry in ??:

$$\begin{aligned} \omega_1(t) &= \frac{c_1}{(c_2 - t)} \wedge \Delta\omega_1(t) = \frac{1}{(c_2 - t)}; \\ \Rightarrow \frac{d\omega_1(t)}{dt} &= \frac{c_1}{(c_2 - t)^2} \wedge \frac{d\Delta\omega_1(t)}{dt} = \frac{1}{(c_2 - t)^2}, \end{aligned}$$

with c_1 and c_2 being constants. This satisfies [equation 9](#):

$$\frac{d\omega_1(t)}{dt} \Delta\omega_1(t) = \frac{c_1}{(c_2 - t)^3} = \frac{d\Delta\omega_1(t)}{dt} \omega_1(t),$$

and [equation 10](#) is again satisfied as:

$$\frac{c_1^2}{(c_2 - t)^2} + \frac{1}{(c_2 - t)^2} \neq 0 \quad \forall t.$$

Conclusion

For the problem, as defined in [equation 8](#), the pulse shapes for a locked effective field strength. In the end, there are two possible solutions, when $\omega_1(t)$ and $\Delta\omega_1(t)$ are not the 0 function and real:

$$\omega_1(t) = c_1 \Delta\omega_1(t), \quad (11)$$

and two special cases of the general solution:

$$\begin{aligned} \omega_1(t) &= c_1 e^{c_2 t}, \frac{c_1}{(c_2 - t)}; \\ \Delta\omega_1(t) &= e^{c_2 t}, \frac{1}{(c_2 - t)}. \end{aligned} \quad (12)$$

A.3. Problem: Constant Effective Field in the Second Rotating Frame

For which amplitude and frequency-modulated RF-pulse shapes is the effective field constant in the second rotating frame constant and holds the following equation:

$$E(t) = \text{const}. \quad (13)$$

Derivation

Start with the problem, a constant field means:

$$\frac{d\varepsilon(t)}{dt} = 0, \quad (14)$$

which is not easy to calculate directly.

First Solution

Take the solution of a constant effective field in the first rotating frame and relate $\omega_{eff}(t)$ and $\frac{d\alpha(t)}{dt}$ with $\omega_1(t)$ and $\Delta\omega_1(t)$ for the effective field in the second rotating frame:

$$\begin{aligned} \omega_{eff}(t) &= c_1 = \sqrt{\omega_1^2(t) + \Delta\omega_1^2(t)}; \\ \frac{d\alpha(t)}{dt} &= c_2. \end{aligned}$$

Integrate $\frac{d\alpha(t)}{dt}$ and take $\alpha(t=0) = 0$:

$$\begin{aligned} \alpha(t) &= \arctan\left(\frac{\omega_1(t)}{\Delta\omega_1(t)}\right) = c_2 t + c_3; \\ \frac{\omega_1(t)}{\Delta\omega_1(t)} &= \tan(c_2 t). \end{aligned}$$

Use ω_{eff} :

$$\Delta\omega_1^2(t) = \frac{c_1^2}{\tan^2(c_2 t) + 1} = c_1^2 \cos^2(c_2 t).$$

Result:

$$\begin{aligned} \omega_1(t) &= c_1 \sin(c_2 t); \\ \Delta\omega_1(t) &= c_1 \cos(c_2 t). \end{aligned}$$

Second Solution

Take the solution of a constant effective field and relate $\omega_{eff}(t)$ and $\frac{d\alpha(t)}{dt}$ with $\omega_1(t)$ and $\Delta\omega_1(t)$:

$$\begin{aligned} \omega_{eff}(t) &= \tanh(2t) = \sqrt{\omega_1^2(t) + \Delta\omega_1^2(t)}; \\ \frac{d\alpha(t)}{dt} &= \frac{1}{\cosh(2t)}. \end{aligned}$$

Integrate $\frac{d\alpha(t)}{dt}$ and take $\alpha(t=0) = 0$:

$$\alpha(t) = \arctan\left(\frac{\omega_1(t)}{\Delta\omega_1(t)}\right) = \arctan(\tanh(t)) + c_3;$$

$$\frac{\omega_1(t)}{\Delta\omega_1(t)} = \tanh(t).$$

Use ω_{eff} :

$$\Delta\omega_1^2(t) = \frac{\tanh^2(2t)}{\tanh^2(t) + 1}.$$

Result:

$$\omega_1(t) = \tanh(t) \frac{\tanh(2t)}{\sqrt{\tanh^2(t) + 1}} = \sinh(t) \frac{\tanh(2t)}{\sqrt{\cosh(2t)}};$$

$$\Delta\omega_1(t) = \frac{\tanh(2t)}{\sqrt{\tanh^2(t) + 1}} = \cosh(t) \frac{\tanh(2t)}{\sqrt{\cosh(2t)}}.$$

Third Solution

Take the solution of a constant effective field and relate $\omega_{eff}(t)$ and $\frac{d\alpha(t)}{dt}$ with $\omega_1(t)$ and $\Delta\omega_1(t)$:

$$\omega_{eff}(t) = c_1 \cos(t) + c_2 \sin(t) = \sqrt{\omega_1^2(t) + \Delta\omega_1^2(t)};$$

$$\frac{d\alpha(t)}{dt} = -c_1 \sin(t) + c_2 \cos(t).$$

Integrate $\frac{d\alpha(t)}{dt}$:

$$\alpha(t) = \arctan\left(\frac{\omega_1(t)}{\Delta\omega_1(t)}\right) = c_1 \cos(t) + c_2 \sin(t) + c_3;$$

$$\frac{\omega_1(t)}{\Delta\omega_1(t)} = \tan(c_1 \cos(t) + c_2 \sin(t)).$$

Use ω_{eff} :

$$\Delta\omega_1^2(t) = \frac{(c_1 \cos(t) + c_2 \sin(t))^2}{\tan^2(c_1 \cos(t) + c_2 \sin(t)) + 1} = (c_1 \cos(t) + c_2 \sin(t))^2 \cos^2(c_1 \cos(t) + c_2 \sin(t)).$$

Result:

$$\omega_1(t) = \tan(c_1 \cos(t) + c_2 \sin(t))(c_1 \cos(t) + c_2 \sin(t)) \cos(c_1 \cos(t) + c_2 \sin(t));$$

$$\Delta\omega_1(t) = (c_1 \cos(t) + c_2 \sin(t)) \cos(c_1 \cos(t) + c_2 \sin(t)).$$

Conclusion

For the problem, as defined in [equation 13](#), the pulse shapes for a constant fictitious field.

In the end, there are two possible solutions, when $\omega_1(t)$ and $\Delta\omega_1(t)$ are not the 0 function and real:

$$\omega_1(t) = c_1 \sin(c_2 t), \sinh(t) \frac{\tanh(2t)}{\sqrt{\cosh(2t)}};$$

$$\Delta\omega_1(t) = c_1 \cos(c_2 t), \cosh(t) \frac{\tanh(2t)}{\sqrt{\cosh(2t)}}. \quad (15)$$

$$\omega_{eff}(t) = c_1 \cos(t) + c_2 \sin(t);$$

$$\omega_1(t) = \omega_{eff}(t) \tan(\omega_{eff}(t)) \cos(\omega_{eff}(t)); \quad (16)$$

$$\Delta\omega_1(t) = \omega_{eff}(t) \cos(\omega_{eff}(t)).$$

A.4. Problem: Equally Effective and Fictitious Field Strength or a Locked E-field

For which amplitude and frequency-modulated RF-pulse shapes have the effective and fictitious field an equal strength and holds the following equation:

$$B_{eff}(t) = \gamma^{-1} \frac{d\alpha(t)}{dt}. \quad (17)$$

Derivation

Start with the problem:

$$B_{eff}(t) = \gamma^{-1} \sqrt{\omega_1^2(t) + \Delta\omega_1^2(t)} = \gamma^{-1} \frac{d\alpha(t)}{dt} = \gamma^{-1} \frac{\frac{d\omega_1(t)}{dt} \Delta\omega_1(t) - \frac{d\Delta\omega_1(t)}{dt} \omega_1(t)}{\omega_1^2(t) + \Delta\omega_1^2(t)}.$$

Special Case

The first solution of [equation 17](#):

$$\omega_1(t) = -c_1 \cos(c_2 t) \wedge \Delta\omega_1(t) = c_1 \sin(c_2 t).$$

Another Special Case

Rewritten the problem:

$$\int \sqrt{\omega_1^2(t) + \Delta\omega_1^2(t)} dt = \arctan\left(\frac{\omega_1(t)}{\Delta\omega_1(t)}\right).$$

Proposing an intermediate solution:

$$\int \frac{1}{\cosh(2t)} dt = \arctan(\tanh(t)).$$

This results in the following equations:

$$\begin{aligned} \sqrt{\omega_1^2(t) + \Delta\omega_1^2(t)} &= \frac{1}{\cosh(2t)}; \\ \frac{\omega_1(t)}{\Delta\omega_1(t)} &= \tanh(t). \end{aligned}$$

Solve for $\omega_1(t)$ and $\Delta\omega_1(t)$:

$$\begin{aligned} \omega_1^2(t) + \Delta\omega_1^2(t) &= \frac{1}{\cosh^2(2t)}; \\ \Rightarrow \Delta\omega_1^2(t) &= \frac{1}{\cosh^2(2t)} \frac{1}{1 + \tanh^2(t)} = \frac{\cosh^2(t)}{\cosh^2(2t)}. \end{aligned}$$

The final solution:

$$\begin{aligned} \omega_1(t) &= \frac{\sinh(t)}{\sqrt{\cosh^3(2t)}}; \\ \Delta\omega_1(t) &= \frac{\cosh(t)}{\sqrt{\cosh^3(2t)}}. \end{aligned}$$

Conclusion

For the problem, as defined in [equation 17](#), the pulse shapes for a constant fictitious field.

In the end, there are two possible solutions, when $\omega_1(t)$ and $\Delta\omega_1(t)$ are not the 0 function and real:

$$\begin{aligned} \omega_1(t) &= -c_1 \cos(c_2 t); \\ \Delta\omega_1(t) &= c_1 \sin(c_2 t). \end{aligned} \quad (18)$$

$$\begin{aligned} \omega_1(t) &= \frac{\sinh(t)}{\sqrt{\cosh^3(2t)}}; \\ \Delta\omega_1(t) &= \frac{\cosh(t)}{\sqrt{\cosh^3(2t)}}. \end{aligned} \quad (19)$$